

# On Green's function retrieval by iterative substitution of the coupled Marchenko equations

Joost van der Neut,<sup>1</sup> Ivan Vasconcelos<sup>2</sup> and Kees Wapenaar<sup>1</sup>

<sup>1</sup>Department of Geoscience and Engineering, Delft University of Technology, Stevinweg 1, 2628 CN Delft, The Netherlands. E-mail: j.r.vanderneut@tudelft.nl

<sup>2</sup>Schlumberger Gould Research, High Cross, Madingley Road, Cambridge CB3 0EL, United Kingdom

Accepted 2015 August 7. Received 2015 August 7; in original form 2015 January 6

## SUMMARY

Iterative substitution of the coupled Marchenko equations is a novel methodology to retrieve the Green's functions from a source or receiver array at an acquisition surface to an arbitrary location in an acoustic medium. The methodology requires as input the single-sided reflection response at the acquisition surface and an initial focusing function, being the time-reversed direct wavefield from the acquisition surface to a specified location in the subsurface. We express the iterative scheme that is applied by this methodology explicitly as the successive actions of various linear operators, acting on an initial focusing function. These operators involve multidimensional crosscorrelations with the reflection data and truncations in time. We offer physical interpretations of the multidimensional crosscorrelations by subtracting traveltimes along common ray paths at the stationary points of the underlying integrals. This provides a clear understanding of how individual events are retrieved by the scheme. Our interpretation also exposes some of the scheme's limitations in terms of what can be retrieved in case of a finite recording aperture. Green's function retrieval is only successful if the relevant stationary points are sampled. As a consequence, internal multiples can only be retrieved at a subsurface location with a particular ray parameter if this location is illuminated by the direct wavefield with this specific ray parameter. Several assumptions are required to solve the Marchenko equations. We show that these assumptions are not always satisfied in arbitrary heterogeneous media, which can result in incomplete Green's function retrieval and the emergence of artefacts. Despite these limitations, accurate Green's functions can often be retrieved by the iterative scheme, which is highly relevant for seismic imaging and inversion of internal multiple reflections.

**Key words:** Controlled source seismology; Wave scattering and diffraction.

## 1 INTRODUCTION

Strong heterogeneities in the shallow subsurface can distort transmitted seismic wavefields, thereby challenging the imaging, characterization or monitoring of deep targets from the acquisition surface. To overcome this problem, the seismic wavefield can be redatumed to a level below the major complexities (Berryhill 1984). Such redatuming requires an estimate of the transmission response of the overburden, which can either be computed in a macro velocity model of the subsurface or be retrieved directly from the reflection data, using for instance the Common Focal Point (CFP) method (Al-Ali & Verschuur 2006). Although this type of redatuming addresses the propagation effects through the overburden, internal multiple reflections are not taken into account.

Bakulin & Calvert (2006) revised the seismic redatuming problem by deploying actual receivers below the overburden that mea-

sure the transmission response directly. In their so-called virtual source method, this transmission response is used for data-driven redatuming. Similar concepts have been presented by Schuster (2009) and various others, inspired by the principles of seismic interferometry. The original aim of the virtual source method has been to correct only for the primary transmission effects of the overburden. Since internal multiple reflections were not accounted for in the formulation, spurious events could emerge in the retrieved gathers (Snieder *et al.* 2006). This problem has been mitigated to some extent by separating upgoing and downgoing waves prior to redatuming, which was made possible by the deployment of multicomponent receivers (Mehta *et al.* 2007). Wapenaar *et al.* (2011) demonstrated that redatuming of the complete wavefield can be achieved by multidimensional deconvolution of the separated wavefields. To establish this technology, knowledge was required of the Green's functions (including all orders of internal multiples) as they would be recorded at depth due to sources at the surface. So far, this could only be

achieved by deploying physical multicomponent receivers in the subsurface.

Recently, a novel iterative scheme was presented to retrieve the required Green's functions from reflection data and an estimate of the propagation effect of the direct wavefield through the overburden (Wapenaar *et al.* 2014b). This estimate can be obtained from a macro velocity model, but a CFP operator may also be used. The development of this methodology has been inspired by the pioneering work of Rose (2002). Brogini & Snieder (2012) related this work to seismic interferometry, from where it was realized how a Green's function of a 1-D medium can be retrieved from its single-sided reflection response. This methodology was extended to 3-D wave propagation by Wapenaar *et al.* (2014b), relying on a causality assumption that is satisfied in media with moderately curved interfaces, but whose limitations are still to be investigated in more complex media. In this paper, we restrict ourselves to applications in acoustic media. Extensions of the methodology for elastodynamic wave propagation have been presented by da Costa Filho *et al.* (2014) and Wapenaar & Slob (2014).

In the so-called Marchenko redatuming (Wapenaar *et al.* 2014a), the estimated Green's functions are used to redatum the seismic wavefield, potentially below a complex overburden. Since internal multiple reflections are included in the estimated transmission response, they are correctly handled by this methodology. Marchenko redatuming can also be used directly for imaging. By applying the methodology at each depth level in the subsurface and taking the response at zero time lag and zero space lag, an image with accurate amplitudes can be obtained without artefacts from internal multiple reflections (Wapenaar *et al.* 2014a; Brogini *et al.* 2014a; Behura *et al.* 2014). By including non-zero lags, equivalent extended images can also be created (Vasconcelos & Rickett 2013), which can be useful input for migration velocity analysis (Sava & Vasconcelos 2011), reservoir characterization (De Bruin *et al.* 1990; Thomson 2012) and novel schemes for nonlinear imaging (Fleury & Vasconcelos 2012; Ravasi & Curtis 2012) and waveform inversion (Vasconcelos *et al.* 2014a). Alternatively, we can use the Marchenko equations to retrieve internal multiples at the acquisition level, which could then be adaptively subtracted from the recorded data (Meles *et al.* 2015). For some initial field data applications of Marchenko redatuming, see Ravasi *et al.* (2015) and Van der Neut *et al.* (2015b).

In this paper, we provide an alternative view on Green's function retrieval by explicit iterative substitution of the coupled Marchenko equations, following Wapenaar *et al.* (2014b) and Slob *et al.* (2014). We build on knowledge and findings of seismic interferometry, where the retrieval of a seismic response through crosscorrelation is commonly interpreted by subtracting traveltimes along common ray paths at the stationary points of the underlying integrals (Schuster 2009). Since the iterative scheme that we consider can be interpreted as a sequential series of crosscorrelations, this interpretation provides us with valuable insights on how individual events in the retrieved Green's functions are constructed. We begin the paper with a concise derivation of the Green's function representations that undergird the coupled Marchenko equations. Then, we introduce a discrete framework in which the coupled Marchenko equations can be effectively represented and solved. We study the retrieval of Green's function in a layered medium and in a medium with point scatterers. Based on our observations, several conclusions will be drawn on the requirements and limitations of the methodology.

## 2 GREEN'S FUNCTION REPRESENTATIONS

An extensive derivation of the coupled Marchenko equations for acoustic wave propagation in 3-D media with smooth moderately curved interfaces is given by Wapenaar *et al.* (2014b). In this section, we introduce an alternative derivation that requires less steps but provides additional physical insights. In both derivations, an essential role is played by the so-called focusing functions, relating the desired Green's functions in the subsurface directly to the recorded data at the surface. While Wapenaar *et al.* (2014b) define these focusing functions as solutions of the wave equation with a specified focusing condition, we define them in this paper as functions of transmission and reflection responses. However, since the origin of both derivations is found in the same reciprocity theorems for one-way wavefields, the results are effectively the same. We start this section with an introduction to the required reciprocity theorems. Then, we introduce two focusing functions: one for focusing at depth and the other for focusing at the acquisition surface.

### 2.1 Reciprocity theorems

Throughout this paper, we express wavefields in the time-space domain as  $p(\boldsymbol{\chi}, z; t)$ . In this notation,  $t$  and  $z$  denote the time and depth, while  $\boldsymbol{\chi}$  refers to the horizontal ( $x$  and  $y$ ) coordinates of space. Further, we define  $\mathbf{x} = (x, y, z) = (\boldsymbol{\chi}, z)$ . Bold characters are used to denote vectors and matrices, whereas all scalars are non-bold. Any wavefield can be transformed to the frequency-space domain by the temporal Fourier transform that we define as

$$\hat{p}(\boldsymbol{\chi}, z; \omega) = \int_{-\infty}^{+\infty} dt \exp(-j\omega t) p(\boldsymbol{\chi}, z; t). \quad (1)$$

Here, the hat denotes the frequency-space domain,  $j$  is the imaginary unit and  $\omega$  is the angular frequency. The inverse Fourier transform is defined as

$$p(\boldsymbol{\chi}, z; t) = \frac{1}{2\pi} \int_{-\infty}^{+\infty} d\omega \exp(j\omega t) \hat{p}(\boldsymbol{\chi}, z; \omega). \quad (2)$$

In reciprocity theorems for one-way wavefields (Wapenaar & Grimbergen 1996), wavefields are defined in two states A and B (indicated by subscripts  $A$  and  $B$ ) in the frequency-space domain. These wavefields are evaluated at two depth levels, being the acquisition surface  $\Lambda_a$  and the focusing level  $\Lambda_f$ . The wavefields are decomposed into downgoing and upgoing constituents, where downgoing is indicated with superscript  $+$  and upgoing with superscript  $-$ . The decomposed wavefields are flux-normalized (Corones *et al.* 1983; Fishman *et al.* 1987) and can be related to the physical quantities of pressure and vertical particle velocity, using expressions of Wapenaar & Grimbergen (1996). We note that the coordinate system can be rotated and that reciprocity theorems for one-way wavefields have also been defined in curvilinear coordinate systems (Frijlink & Wapenaar 2010). Hence, the following theory may also be extended for such coordinate systems.

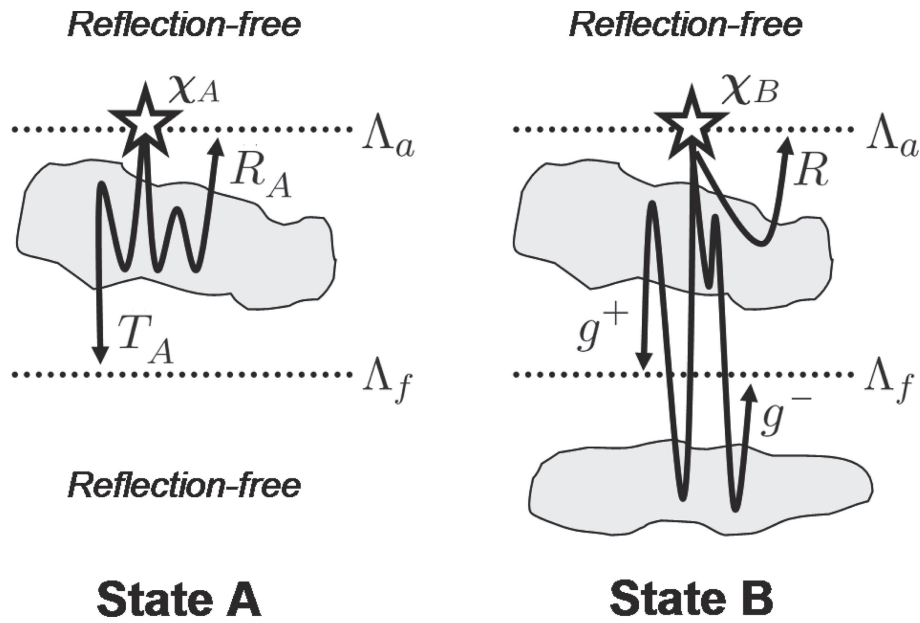


**Figure 1.** Illustration of states A and B that are discussed in the main text. Levels  $\Lambda_a$  and  $\Lambda_f$  are infinitely long boundaries. In both states, the medium properties are identical to the physical medium between these boundaries and the medium is reflection free above  $\Lambda_a$ . In state A, the medium is also reflection free below  $\Lambda_f$ , whereas in state B, it is identical to the physical medium below this boundary.

We start with a reciprocity theorem of the convolution type, relating two wavefields that are propagating forward in time (Wapenaar & Grimbergen 1996):

$$\int_{\Lambda_a} d^2\chi \{ \hat{p}_A^+ \hat{p}_B^- - \hat{p}_A^- \hat{p}_B^+ \} = \int_{\Lambda_f} d^2\chi \{ \hat{p}_A^+ \hat{p}_B^- - \hat{p}_A^- \hat{p}_B^+ \}. \quad (3)$$

Because all wavefield quantities are expressed in the frequency-space domain, the multiplications in eq. (3) are equivalent to convolutions in the time-space domain. The integrals are carried out over level  $\Lambda_a$  at depth  $z_a$  and level  $\Lambda_f$  at depth  $z_f$ . Eq. (3) is valid when the medium parameters between  $\Lambda_a$  and  $\Lambda_f$  are identical in both states and when no sources exist between these depth levels. The medium parameters of both states can be different from each other above  $\Lambda_a$  and below  $\Lambda_f$ . Sources can also exist in this part of the medium.

An analogous reciprocity theorem of the correlation type relates wavefields that propagate forward in time to wavefields that propagate backward in time (Wapenaar & Grimbergen 1996):

$$\int_{\Lambda_a} d^2\chi \{ \hat{p}_A^+ \hat{p}_B^{+*} - \hat{p}_A^- \hat{p}_B^{-*} \} = \int_{\Lambda_f} d^2\chi \{ \hat{p}_A^+ \hat{p}_B^{+*} - \hat{p}_A^- \hat{p}_B^{-*} \}. \quad (4)$$

Here, the superscript  $*$  denotes complex conjugation, being equivalent to time reversal in the time-space domain. Hence, the multiplications in eq. (4) are crosscorrelations in the time-space domain. Apart from the assumptions that are intrinsic to the reciprocity theorem of the convolution type, eq. (4) requires the medium to be lossless between the levels  $\Lambda_a$  and  $\Lambda_f$ . This requirement imposes an important limitation to the current methodology, namely that intrinsic losses in the overburden are not accounted for in the underlying theory. Moreover, evanescent wave modes are ignored at  $\Lambda_a$  and  $\Lambda_f$ .

### 2.2 Focusing at depth

We will choose a medium A in state A that is identical to the physical medium above  $\Lambda_f$  and reflection-free below this level. We refer to

this truncated medium with subscript A. For state B, we choose the physical medium (referred to without a subscript). An illustration is given in Fig. 1. In both states, we do not include a free surface (i.e. no downgoing waves exist at or above  $\Lambda_a$ ). Free-surface multiples can also be included, yielding an additional integral in the Green's function representations and the coupled Marchenko equations that follow (Singh *et al.* 2015).

In state A, we place a point source for a downgoing wavefield just above  $\Lambda_a$ , creating a delta function in the lateral coordinates at  $\Lambda_a$ , that is  $\hat{p}_A^+ = \delta(\chi - \chi_A)$ . Here,  $\chi_A$  is the horizontal location of the source, which is positioned at depth  $z_a$ . The upgoing wavefield at  $\Lambda_a$  is  $\hat{p}_A^- = \hat{R}_A(\chi, z_a; \chi_A, z_a; \omega)$ , being the reflection response at the surface in the truncated medium. At  $\Lambda_f$ , we find the downgoing wavefield  $\hat{p}_A^+ = \hat{T}_A(\chi, z_f; \chi_A, z_a; \omega)$ , being the transmission response of the truncated medium. Since the medium is non-reflective below  $\Lambda_f$ , the upgoing wavefield at this level is  $\hat{p}_A^- = 0$ . In state B, we also place a point source for a downgoing wavefield (at  $\chi_B$ ) just above the surface, such that  $\hat{p}_B^+ = \delta(\chi - \chi_B)$  and  $\hat{p}_B^- = \hat{R}(\chi, z_a; \chi_B, z_a; \omega)$ , being the reflection response of the physical medium at the surface. At the focusing level, we refer to the wavefields in state B as downgoing and upgoing Green's functions  $\hat{p}_B^\pm = \hat{G}^\pm(\chi, z_f; \chi_B, z_a; \omega)$ . Substituting these ingredients into eqs (3) and (4) brings us (after re-arranging some terms) at

$$\int_{\Lambda_f} d^2\chi \hat{T}_A(\chi, z_f; \chi_A, z_a; \omega) \hat{G}^-(\chi, z_f; \chi_B, z_a; \omega) = \hat{R}(\chi_A, z_a; \chi_B, z_a; \omega) - \hat{R}_A(\chi_B, z_a; \chi_A, z_a; \omega), \quad (5)$$

and

$$\int_{\Lambda_f} d^2\chi \hat{T}_A(\chi, z_f; \chi_A, z_a; \omega) \hat{G}^{+*}(\chi, z_f; \chi_B, z_a; \omega) = - \int_{\Lambda_a} d^2\chi \hat{R}_A(\chi, z_a; \chi_A, z_a; \omega) \hat{R}^*(\chi, z_a; \chi_B, z_a; \omega) + \delta(\chi_B - \chi_A). \quad (6)$$

To retrieve the Green's function, the inverse of the transmission response  $\hat{T}_A$  should be applied to eqs (5) and (6). Initially, this inverse is unknown, but, as we will see later, it can be retrieved by an iterative scheme. We refer to the inverse of  $\hat{T}_A$  as  $\hat{f}_1^+$ , which is defined via

$$\delta(\boldsymbol{\chi} - \boldsymbol{\chi}_F) = \int_{\Lambda_a} d^2 \boldsymbol{\chi}_A \hat{T}_A(\boldsymbol{\chi}, z_f, \boldsymbol{\chi}_A, z_a; \omega) \times \hat{f}_1^+(\boldsymbol{\chi}_A, z_a; \boldsymbol{\chi}_F, z_f; \omega). \quad (7)$$

The delta function should be interpreted as a spatially band-limited delta function, where the evanescent field has been ignored (Wapenaar *et al.* 2014b). The field  $\hat{f}_1^+$  is identical to the downgoing part of the focusing function  $\hat{f}_1$ , as defined by Wapenaar *et al.* (2014b), being a solution of the wave equation in the truncated medium with a specified focusing condition.

By applying  $\hat{f}_1^+(\boldsymbol{\chi}_A, z_a; \boldsymbol{\chi}_F, z_f; \omega)$  to eqs (5) and (6), we find, after integrating  $\boldsymbol{\chi}_A$  over  $\Lambda_a$  and with help of eq. (7):

$$\hat{G}^-(\boldsymbol{\chi}_F, z_f; \boldsymbol{\chi}_B, z_a; \omega) = \int_{\Lambda_a} d^2 \boldsymbol{\chi} \hat{R}(\boldsymbol{\chi}, z_a; \boldsymbol{\chi}_B, z_a; \omega) \times \hat{f}_1^+(\boldsymbol{\chi}, z_a; \boldsymbol{\chi}_F, z_f; \omega) - \hat{f}_1^-(\boldsymbol{\chi}_B, z_a; \boldsymbol{\chi}_F, z_f; \omega), \quad (8)$$

and

$$\hat{G}^{+*}(\boldsymbol{\chi}_F, z_f; \boldsymbol{\chi}_B, z_a; \omega) = - \int_{\Lambda_a} d^2 \boldsymbol{\chi} \hat{R}^*(\boldsymbol{\chi}, z_a; \boldsymbol{\chi}_B, z_a; \omega) \times \hat{f}_1^-(\boldsymbol{\chi}, z_a; \boldsymbol{\chi}_F, z_f; \omega) + \hat{f}_1^+(\boldsymbol{\chi}_B, z_a; \boldsymbol{\chi}_F, z_f; \omega). \quad (9)$$

For notational convenience, we have replaced the integration variable  $\boldsymbol{\chi}_A$  in eq. (8) by  $\boldsymbol{\chi}$ , and we defined additionally

$$\hat{f}_1^-(\boldsymbol{\chi}, z_a; \boldsymbol{\chi}_F, z_f; \omega) = \int_{\Lambda_a} d^2 \boldsymbol{\chi}_A \hat{R}_A(\boldsymbol{\chi}, z_a; \boldsymbol{\chi}_A, z_a; \omega) \times \hat{f}_1^+(\boldsymbol{\chi}_A, z_a; \boldsymbol{\chi}_F, z_f; \omega), \quad (10)$$

which can be interpreted as the response of the truncated medium to  $\hat{f}_1^+$ . Note that  $\hat{f}_1^-$  is the upgoing part of the focusing function as defined by Wapenaar *et al.* (2014b), where  $\hat{f}_1 = \hat{f}_1^+ + \hat{f}_1^-$ . Eqs (8) and (9) are essential representations that will be utilized later to retrieve the Green's functions  $\hat{G}^-$  and  $\hat{G}^{+*}$ .

### 2.3 Focusing at the acquisition level

Remember that  $\hat{f}_1^+$  is defined as the inverse of the transmission response from level  $\Lambda_a$  to  $\Lambda_f$ , where  $\Lambda_a$  is the integration surface (see eq. 7). Alternatively, we can define a focusing function  $\hat{f}_2^-$  as the inverse of the transmission response from level  $\Lambda_f$  to  $\Lambda_a$ , where  $\Lambda_f$  is the integration surface. For this purpose, we introduce

$$\delta(\boldsymbol{\chi} - \boldsymbol{\chi}_B) = \int_{\Lambda_f} d^2 \boldsymbol{\chi}_G \hat{T}_A(\boldsymbol{\chi}, z_a; \boldsymbol{\chi}_G, z_f; \omega) \times \hat{f}_2^-(\boldsymbol{\chi}_G, z_f; \boldsymbol{\chi}_B, z_a; \omega). \quad (11)$$

In this expression,  $\hat{T}_A$  is the transmission response of the truncated medium when illuminated from below and  $\hat{f}_2^-$  is its inverse. Similar to  $\hat{f}_1^-$ , we can define  $\hat{f}_2^+$  as the response of the truncated medium to  $\hat{f}_2^-$ , according to

$$\hat{f}_2^+(\boldsymbol{\chi}, z_f; \boldsymbol{\chi}_B, z_a; \omega) = \int_{\Lambda_f} d^2 \boldsymbol{\chi}_G \hat{R}_A^\circ(\boldsymbol{\chi}, z_f; \boldsymbol{\chi}_G, z_f; \omega) \times \hat{f}_2^-(\boldsymbol{\chi}_G, z_f; \boldsymbol{\chi}_B, z_a; \omega), \quad (12)$$

where  $\hat{R}_A^\circ$  is introduced as the reflection response of the truncated medium from below.

Wapenaar *et al.* (2014b) showed that  $\hat{f}_1^\pm$  and  $\hat{f}_2^\pm$  obey the following relations:

$$\hat{f}_1^+(\boldsymbol{\chi}_B, z_a; \boldsymbol{\chi}_F, z_f; \omega) = \hat{f}_2^-(\boldsymbol{\chi}_F, z_f; \boldsymbol{\chi}_B, z_a; \omega), \quad (13)$$

and

$$- \hat{f}_1^{-*}(\boldsymbol{\chi}_B, z_a; \boldsymbol{\chi}_F, z_f; \omega) = \hat{f}_2^+(\boldsymbol{\chi}_F, z_f; \boldsymbol{\chi}_B, z_a; \omega). \quad (14)$$

These relations follow directly from the definitions (7) and (11), and the symmetry of the transmission response. They play an essential role in the reasoning that will be applied in the following section.

## 3 THE COUPLED MARCHENKO EQUATIONS

To derive the coupled Marchenko equations, we rewrite eqs (8) and (9) in a discrete notation. Then, we introduce a causality argument, which is imposed by a window matrix. Having derived the coupled Marchenko equations, they can be solved by iterative substitution. Eventually, the desired Green's functions can be computed.

### 3.1 Discrete notation

For the introduction of our discrete notation, we start by rewriting eqs (8) and (9) in the time–space domain. This is done by substituting the forward Fourier transform of  $\hat{f}_1^+$  (as in eq. 1) into eq. (8). We apply inverse Fourier transformation with eq. (2) to both sides of the result. After rearranging the terms, we find

$$\hat{f}_1^-(\boldsymbol{\chi}_B, z_a; \boldsymbol{\chi}_F, z_f; t) + G^-(\boldsymbol{\chi}_F, z_f; \boldsymbol{\chi}_B, z_a; t) = \left[ \frac{1}{2\pi} \int_{-\infty}^{+\infty} d\omega \exp(j\omega t) \int_{\Lambda_a} d^2 \boldsymbol{\chi} \hat{R}(\boldsymbol{\chi}, z_a; \boldsymbol{\chi}_B, z_a; \omega) \times \int_{-\infty}^{+\infty} d\tau \exp(-j\omega\tau) \right] \hat{f}_1^+(\boldsymbol{\chi}, z_a; \boldsymbol{\chi}_F, z_f; \tau) \quad (15)$$

The term between square brackets can be interpreted as a multidimensional filter, acting on the downgoing focusing function  $\hat{f}_1^+(\boldsymbol{\chi}, z_a; \boldsymbol{\chi}_F, z_f; \tau)$ . We introduced  $\tau$  as an additional time variable. For practical reasons, we prefer to rewrite this expression in a discrete and concise way. For this purpose, we store the focusing functions as vectors  $\mathbf{f}_1^\pm$  in which the seismic traces are concatenated in the time–space domain. Further, we define a matrix  $\mathbf{R}$  that applies the operations between the square brackets in eq. (15), meaning forward Fourier transformation, multidimensional convolution with the reflection response and inverse Fourier transformation. Effectively, this filter propagates the downgoing focusing function forward in time with the reflection response. As can be observed from eq. (15), this operation yields, besides the upgoing focusing function  $\hat{f}_1^-$ , the

upgoing Green's function  $G^-$ . This Green's function is written as a vector  $\mathbf{g}^-$ . Here, it should be noted that the organization of the elements in this vector with respect to  $\chi_B$  and  $t$  is similar as in the focusing functions  $\mathbf{f}_1^+$ . Within this discrete framework, eq. (15) can be written for any focal point as

$$\mathbf{f}_1^- + \mathbf{g}^- = \mathbf{R}\mathbf{f}_1^+. \quad (16)$$

Eq. (9) can be rewritten in a similar way. This is done by substitution of the forward Fourier transform of  $f_1^-$  (as in eq. 1). After inverse Fourier transformation of the result with eq. (2) and rearranging the terms, we find

$$\begin{aligned} & f_1^+(\chi_B, z_a; \chi_F, z_f; t) - G^+(\chi_F, z_f; \chi_B, z_a; -t) \\ &= \left[ \frac{1}{2\pi} \int_{-\infty}^{+\infty} d\omega \exp(j\omega t) \int_{\Lambda_a} d^2\chi \hat{R}^*(\chi, z_a; \chi_B, z_a; \omega) \right. \\ & \quad \left. \times \int_{-\infty}^{+\infty} d\tau \exp(-j\omega\tau) \right] f_1^-(\chi, z_a; \chi_F, z_f; \tau). \end{aligned} \quad (17)$$

The term between square brackets can be interpreted as a multidimensional filter, propagating the upgoing focusing function backward in time with the reflection response. We introduce matrix  $\mathbf{R}^*$  that applies this operation to any vector. The action of  $\mathbf{R}^*$  on  $\mathbf{f}_1^-$  yields, besides the downgoing focusing function, the downgoing Green's function  $-\mathbf{g}^{+*}$ , propagating backward in time with reversed polarity. Here, it should be noted that the organization of the elements in this vector with respect to  $\chi_B$  and  $t$  is similar as in the focusing functions, but that all traces are reversed in time (which is indicated by superscript  $\star$ ). With these ingredients, eq. (17) can be written as

$$\mathbf{f}_1^+ - \mathbf{g}^{+*} = \mathbf{R}^*\mathbf{f}_1^-. \quad (18)$$

On the right-hand side of eqs (16) and (18), we find multidimensional filters that propagate the focusing functions forward and backward in time. On the left-hand side, we find a constituent of the Green's function and a constituent of the focusing function. Our aim is to solve these two equations having four unknowns ( $\mathbf{g}^{+*}$ ,  $\mathbf{g}^-$ ,  $\mathbf{f}_1^+$  and  $\mathbf{f}_1^-$ ). Hence, in its present form, this system of equations is underdetermined. However, we can eliminate two unknowns by exploiting the fact that focusing functions and Green's functions have different causality properties in the time-space domain.

### 3.2 The window matrix

We assume that the Green's function contains a distinct downgoing direct arrival and a coda of reflected events that arrive thereafter. We design a window matrix  $\Theta$  that removes all events after the direct wave, including the direct wave itself. This window is designed to be symmetric in time. Hence, any acausal event that arrives before the time-reversed direct wave is also removed by its action. When  $\Theta$  is applied to the upgoing Green's function  $\mathbf{g}^-$ , causality dictates that

$$\Theta\mathbf{g}^- = \mathbf{0}. \quad (19)$$

Since  $\Theta$  is symmetric in time, it follows for the time-reversed downgoing Green's function  $\mathbf{g}^{+*}$  that

$$\Theta\mathbf{g}^{+*} = \mathbf{0}. \quad (20)$$

Hence, the Green's functions can be eliminated from eqs (16) and (18) by applying matrix  $\Theta$ .

In the following, we analyse how the focusing functions that also appear in the left-hand side of eqs (16) and (18) respond to the actions of  $\Theta$ . For this purpose, we make use of eq. (7). We rewrite this equation in the time-space domain by substituting the forward Fourier transform (as in eq. 1) of  $f_1^+$  and applying inverse Fourier transformation (as in eq. 2) to both sides of the result, yielding

$$\begin{aligned} & \delta(\chi - \chi_F)\delta(t) \\ &= \left[ \frac{1}{2\pi} \int_{-\infty}^{+\infty} d\omega \exp(j\omega t) \int_{\Lambda_a} d^2\chi_A \hat{T}_A(\chi, z_f; \chi_A, z_a; \omega) \right. \\ & \quad \left. \times \int_{-\infty}^{+\infty} d\tau \exp(-j\omega\tau) \right] f_1^+(\chi_A, z_a; \chi_F, z_f; \tau). \end{aligned} \quad (21)$$

The term between square brackets can be interpreted as a multidimensional filter, acting on the downgoing focusing function. This filter can also be represented by matrix  $\mathbf{T}_A$ , acting on the vectorized focusing function  $\mathbf{f}_1^+$ . The term on the left-hand side can be discretely represented by a vector  $\mathbf{i}$ , having only one non-zero element at  $t = 0$  and  $\chi = \chi_F$  at the chosen focusing location. With these definitions, eq. (21) can be written as

$$\mathbf{i} = \mathbf{T}_A\mathbf{f}_1^+. \quad (22)$$

Remember that we assume the transmission response to contain a direct wave and a distinct coda that arrives thereafter. Building on this assumption, matrix  $\mathbf{T}_A$  can be partitioned as

$$\mathbf{T}_A = \mathbf{T}_{Ad} + \mathbf{T}_{Am}, \quad (23)$$

where  $\mathbf{T}_{Ad}$  describes the convolution with the direct wave and  $\mathbf{T}_{Am}$  describes the convolution with the coda, resulting from internal multiple reflections in the transmission response. We define a focusing function for the direct wave  $\mathbf{f}_{1d}^+$ , which will be referred to as the initial focusing function. In analogy to eq. (22), the initial focusing function obeys

$$\mathbf{i} = \mathbf{T}_{Ad}\mathbf{f}_{1d}^+. \quad (24)$$

The initial focusing function  $\mathbf{f}_{1d}^+$  can be subtracted from  $\mathbf{f}_1^+$ . We refer to the remainder as the coda  $\mathbf{f}_{1m}^+$ , where

$$\mathbf{f}_1^+ = \mathbf{f}_{1d}^+ + \mathbf{f}_{1m}^+. \quad (25)$$

To investigate the properties of  $\mathbf{f}_{1d}^+$  and  $\mathbf{f}_{1m}^+$ , we subtract eq. (24) from eq. (22). The result is rewritten with help of eqs (23) and (25) as

$$\mathbf{T}_{Am}\mathbf{f}_{1d}^+ = -(\mathbf{T}_{Ad} + \mathbf{T}_{Am})\mathbf{f}_{1m}^+. \quad (26)$$

This result can be interpreted as follows. When  $\mathbf{T}_{Ad}$  is applied to  $\mathbf{f}_{1d}^+$ , it will produce a response at zero intercept time, as dictated by eq. (24). Hence,  $\mathbf{f}_{1d}^+$  should contain a single event that is kinematically identical to the time-reversed direct wave. Since  $\mathbf{T}_{Am}$  applies convolutions with events that arrive after the direct wave, the left-hand side of eq. (26) is purely causal. Hence, the right-hand side should be causal too. The earliest event on the right-hand side is produced by the convolution of the direct wave in  $\mathbf{T}_{Ad}$  with the first event in  $\mathbf{f}_{1m}^+$ . The condition that this event should be causal translates directly in the conclusion that  $\mathbf{f}_{1m}^+$  cannot contain any event arriving earlier than the time-reversed direct wave.

We have thus concluded that the time-reversed direct wave is the earliest event in  $\mathbf{f}_1^+$ . With the help of eq. (13), we can also conclude that the time-reversed direct wave is the earliest event in  $\mathbf{f}_2^-$ . Since eq. (12) states that  $\mathbf{f}_2^+$  can be obtained by convolving  $\mathbf{f}_2^-$  with a causal reflection response, it follows that all events in  $\mathbf{f}_2^+$

arrive after the time-reversed direct wave. Since  $\mathbf{f}_1^-$  is related to  $\mathbf{f}_2^+$  by polarity reversal and time reversal, as dictated by eq. (14), we conclude that all events in  $\mathbf{f}_1^-$  arrive before the direct wave.

Using the causality of the reflection response and the fact that  $\mathbf{f}_1^+$  and  $\mathbf{f}_1^-$  are related by eq. (12), it follows from the previous statements that all events in  $\mathbf{f}_{1m}^+$  and  $\mathbf{f}_1^-$  arrive after the time-reversed direct wave but before the direct wave. Hence, it can be concluded that

$$\Theta \mathbf{f}_1^+ = \Theta (\mathbf{f}_{1d}^+ + \mathbf{f}_{1m}^+) = \mathbf{f}_{1m}^+, \quad (27)$$

and

$$\Theta \mathbf{f}_1^- = \mathbf{f}_1^-. \quad (28)$$

It is important to realize that our arguments to justify eqs (27) and (28) are rather intuitive and strictly valid in 1-D media only. The exact limitations of these arguments in complex 3-D media are still to be explored, see also Vasconcelos *et al.* (2014b).

### 3.3 Iterative solution

Now that we have verified the responses of the Green's functions and focusing functions to the window matrix, we can apply this matrix to eq. (16). With the help of eqs (19), (25) and (28), the result of this operation can be written as

$$\mathbf{f}_1^- = \Theta \mathbf{R} \mathbf{f}_{1d}^+ + \Theta \mathbf{R} \mathbf{f}_{1m}^+. \quad (29)$$

Similarly, we can use eqs (20), (25) and (27) to deduct from the action of  $\Theta$  on eq. (18) that

$$\mathbf{f}_{1m}^+ = \Theta \mathbf{R}^* \mathbf{f}_1^-. \quad (30)$$

Eqs (29) and (30) are the coupled Marchenko equations. We interpret  $\mathbf{f}_{1d}^+$  as the initial focusing function. Assuming that the direct wave is known from either a macro velocity model or the CFP method (Al-Ali & Verschuur 2006), the initial focusing function can be obtained by inversion of eq. (24). In practice, we generally approximate this inverse by time-reversal (Wapenaar *et al.* 2014b). Once  $\mathbf{f}_{1d}^+$  is known, a first estimate of  $\mathbf{f}_1^-$  can be obtained with eq. (29) (with the initial estimate  $\mathbf{f}_{1m}^+ = \mathbf{0}$ ). Now that we have an estimate of  $\mathbf{f}_1^-$ , we can estimate  $\mathbf{f}_{1m}^+$  with eq. (30), evaluate eq. (29) again and proceed by iteration. With every iteration of eq. (29), the focusing function is propagated forward in time, whereas with every iteration of eq. (30), it is propagated backward in time. As will be shown in the examples, each of these cases can be interpreted as a multidimensional crosscorrelation process.

Alternatively, the focusing function can be retrieved by inversion. By composing eq. (29) with  $\Theta \mathbf{R}^*$  and then noting that eq. (30) permits the elimination of  $\mathbf{f}_1^-$ , we find

$$[\mathbf{I} - \Theta \mathbf{R}^* \Theta \mathbf{R}] \mathbf{f}_{1m}^+ = \Theta \mathbf{R}^* \Theta \mathbf{R} \mathbf{f}_{1d}^+. \quad (31)$$

This equation can be solved for  $\mathbf{f}_{1m}^+$ . To establish the relation between solving this inverse problem and iteratively substituting eqs (29) and (30), we observe that eq. (31) is a Fredholm equation of the second kind. It is well known that such an equation can be expanded as a Neumann series (Fokkema & Van den Berg 1993), yielding for the  $K$ th order estimate of  $\mathbf{f}_1^+$ :

$$\mathbf{f}_1^{+(K)} = \sum_{k=0}^K (\Theta \mathbf{R}^* \Theta \mathbf{R})^k \mathbf{f}_{1d}^+. \quad (32)$$

Here, we have added  $\mathbf{f}_{1d}^+$  to the expansion of  $\mathbf{f}_{1m}^+$ , for convenience. The  $K$ th order solution of  $\mathbf{f}_1^-$  can be found by substituting this result into eq. (29), yielding

$$\mathbf{f}_1^{-(K)} = \Theta \mathbf{R} \sum_{k=0}^K (\Theta \mathbf{R}^* \Theta \mathbf{R})^k \mathbf{f}_{1d}^+. \quad (33)$$

It can easily be verified that these results are identical to those obtained by iterative substitution of eqs (29) and (30). Hence, our iterative solution can be interpreted as a Neumann series. Note that convergence is established for such a series, under the condition that  $\|(\Theta \mathbf{R}^* \Theta \mathbf{R})^k \mathbf{f}_{1d}^+\|_2 \rightarrow 0$  as  $k \rightarrow \infty$  (Fokkema & Van den Berg 1993), where subscript 2 denotes the  $\ell_2$ -norm.

### 3.4 Green's function retrieval

Once the focusing functions are found, the upgoing Green's function can be computed with eq. (16). Although accurate Green's functions can be retrieved if sufficient iterations are evaluated (Broggini *et al.* 2014b), we often prefer to keep the number of iterations small. To improve the result in these cases, it can be useful to remove all events before the direct arrival. This is achieved by the filter  $\Psi = \mathbf{I} - \Theta$ , which we apply to both sides of eq. (16). Here,  $\mathbf{I}$  is an identity matrix. Note that  $\Psi$  acts as a filter that removes all events before the direct wave, but not the direct wave. With the help of eqs (19), (25) and (28), we obtain in this way

$$\mathbf{g}^- = \Psi \mathbf{R} \mathbf{f}_{1d}^+ + \Psi \mathbf{R} \mathbf{f}_{1m}^+. \quad (34)$$

Similarly, we apply  $\Psi$  to both sides of the eq. (18) to find for the time-reversed downgoing Green's function:

$$\mathbf{g}^{+*} = \mathbf{f}_{1d}^+ - \Psi \mathbf{R}^* \mathbf{f}_1^-, \quad (35)$$

where we used eqs (20), (25) and (27). In eqs (34) and (35), we have deliberately separated the contributions of the initial focusing functions  $\mathbf{f}_{1d}^+$  from the contributions of its coda, since we will track these contributions individually in the examples that follow.

By substitution of eqs (32) and (33) into eqs (34) and (35), it follows that the retrieved Green's functions can also be expressed in terms of a single (but complicated) filter acting on the initial focusing function. In this way, we come up with the following expressions for the  $K$ th order estimate of the Green's functions (where we also used  $\mathbf{f}_1^+ = \mathbf{f}_{1d}^+ + \mathbf{f}_{1m}^+$ ):

$$\mathbf{g}^{-(K)} = \left[ \Psi \mathbf{R} \sum_{k=0}^K (\Theta \mathbf{R}^* \Theta \mathbf{R})^k \right] \mathbf{f}_{1d}^+, \quad (36)$$

and

$$\mathbf{g}^{+*(K)} = \left[ \mathbf{I} - \Psi \mathbf{R}^* \Theta \mathbf{R} \sum_{k=0}^{K-1} (\Theta \mathbf{R}^* \Theta \mathbf{R})^k \right] \mathbf{f}_{1d}^+, \quad (37)$$

for  $K > 0$ . For  $K = 0$ , we define  $\mathbf{g}^{-(0)} = \Psi \mathbf{R} \mathbf{f}_{1d}^+$  and  $\mathbf{g}^{+*(0)} = \mathbf{f}_{1d}^+$ . Note that  $\mathbf{g}^{-(0)}$  is the upgoing wavefield that is retrieved by standard inverse wavefield extrapolation, while  $\mathbf{g}^{+*(0)}$  is the wavefield that is used to initiate the iterative scheme. It has been shown that all events in the Green's functions can be retrieved with correct amplitudes for  $K \rightarrow \infty$ , given that the initial focusing function obeys eq. (24) (Broggini *et al.* 2014b; Slob *et al.* 2014; Wapenaar *et al.* 2014a). In practice, only a few iterations are generally sufficient to predict the dominant internal multiples in the wavefield with fairly accurate amplitudes, as we will demonstrate in the synthetic examples that follow.

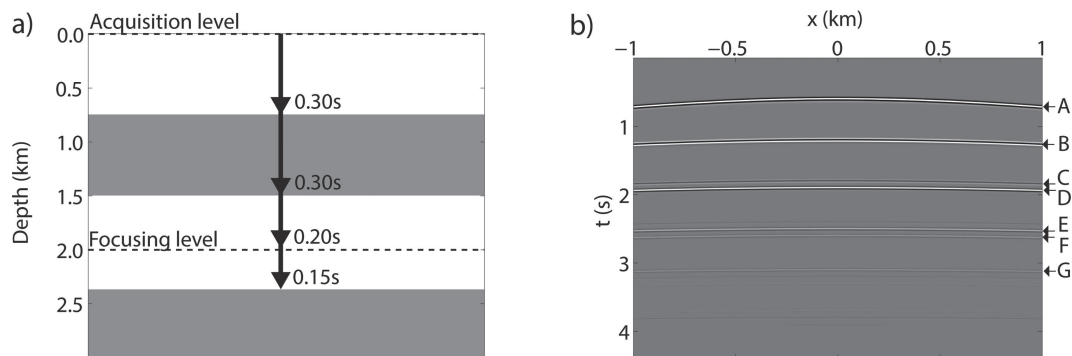


**Figure 2.** (a) Layered model with constant velocity ( $2.5 \text{ km s}^{-1}$ ) and densities of  $1000 \text{ kg m}^{-3}$  (white) and  $2000 \text{ kg m}^{-3}$  (grey). The acquisition level is at 0 km and the focusing level is at 2 km depth. Indicated are the one-way traveltimes at normal incidence between the different interfaces, including the acquisition and focusing levels. (b) Reflection response with a source at  $x = 0 \text{ km}$  at the acquisition level. Various events are labelled.

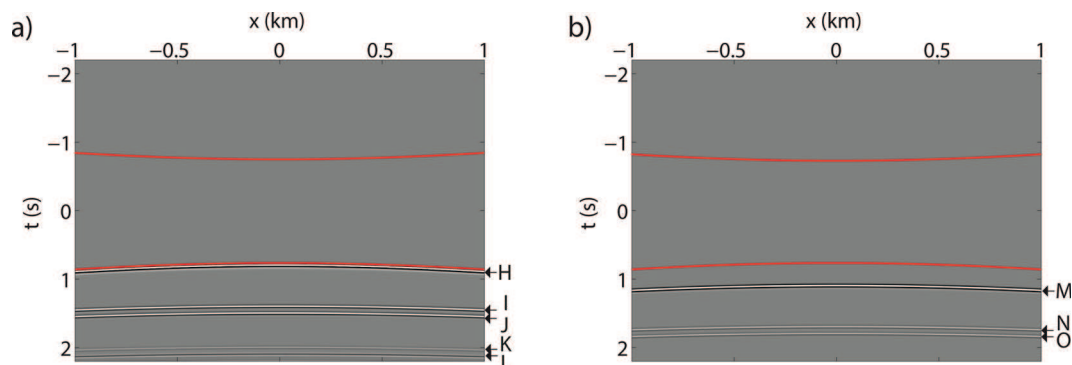


**Figure 3.** (a) Downgoing Green's function. (b) Upgoing Green's function. Both gathers are common receiver gathers that have been obtained by finite difference modelling and wavefield decomposition. Sources are located at the acquisition level and a single receiver is deployed at  $x = 0 \text{ km}$  at the focusing level. The red curves define the muting times for matrix  $\Theta$ .

#### 4 LAYERED MEDIUM EXAMPLE

In this section, we compute synthetic seismic data in a layered medium. To understand the construction of focusing functions when the Marchenko equations are iteratively substituted, we evaluate the result of each iteration individually. Then, we demonstrate how the desired Green's functions are retrieved. Finally, we discuss the existence of stationary points and their locations.

##### 4.1 The model

In Fig. 2(a), we show a simple model with constant velocity of  $2.5 \text{ km s}^{-1}$  and density contrasts at 0.75, 1.5 and 2.375 km. The acquisition level and focusing level are chosen at 0 and 2 km depth, respectively. The model has been designed such that a wave at normal incidence takes 0.3s to reach the first interface, another 0.3s to reach the second interface, another 0.2s to arrive at the focusing level and 0.15s more to get to the deepest interface. These traveltimes have been indicated in the figure for convenience. In Fig. 2(b), we show the reflection response of a single source at the acquisition level. We have identified various events with labels A–G. Our aim is to retrieve the downgoing and upgoing Green's function with sources at the surface and a receiver at the focusing level. In Fig. 3, we show these Green's functions for reference. To obtain these Green's functions, we modelled the responses from every point at the acquisition surface to a virtual array in the subsurface and we applied wavefield decomposition in the frequency–wavenumber domain (Wapenaar *et al.* 2014b). Once more, various events have been identified with labels H–O. Finally, we have drawn a red curve just

above the direct wave and another curve that is mirrored in time. The window matrix  $\Theta$  is designed such that all data outside the two curves are muted, while preserving the data in between the curves.

##### 4.2 Step 1: initiating the upgoing wavefields

The iterative scheme is initiated with the initial focusing function  $\mathbf{f}_{1d}^+$ , which is obtained by time-reversal of the direct wave. This direct wave is indicated as event H in Fig. 3(a). In this stylized example, we isolate this event with a time gate. In practical applications, the direct wave can also be computed by finite-difference modelling in a smooth background model. In the first iteration, we want to update  $\mathbf{f}_1^-$  with eq. (29), using the initial estimate  $\mathbf{f}_{1m}^+ = \mathbf{0}$ . To facilitate this, the initial focusing function is propagated forward in time with the reflection response to compute  $\mathbf{Rf}_{1d}^+$ , as it appears in the right-hand side of eq. (29). Since the initial focusing function is acausal and the reflection response is causal, this operation can be interpreted as a crosscorrelation process. It should be well understood that this is a multidimensional crosscorrelation, since it involves the evaluation of an integral over the acquisition surface (like the integral in eq. 8). This initial step of the scheme is similar to inverse wavefield extrapolation, since it essentially redatums the reflection data at the receiver side (Berryhill 1984). Following similar reasoning as is commonly applied in seismic interferometry (Schuster 2009), each trace in the output gather  $\mathbf{Rf}_{1d}^+$  can be interpreted as the stack of a correlation gather that is obtained by crosscorrelation of each trace in the reflection response at a fixed source point  $\chi_B$  with each trace in the initial focusing function at a fixed focal point  $\chi_F$ . In Fig. 4(a), we show the correlation gather with  $\chi_B$  and  $\chi_F$  both at  $x = 0 \text{ km}$ .

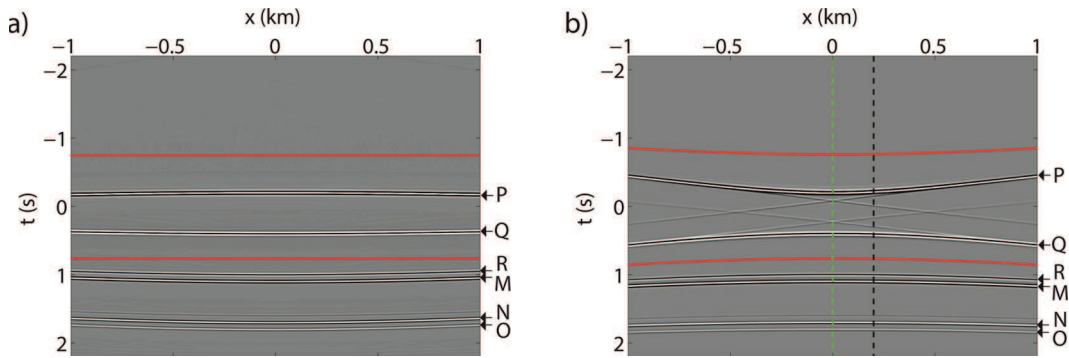


**Figure 4.** (a) Correlation gather of  $\mathbf{Rf}_{1d}^+$  with  $\chi_B$  and  $\chi_F$  both at  $x = 0$  km. (b) Gather of  $\mathbf{Rf}_{1d}^+$  with  $\chi_F$  at  $x = 0$  km. The traces at the dashed green and black lines are constructed by stacking the gathers in panel (a) and Fig. 13(a), respectively. The red curves define the muting times for matrix  $\Theta$ .

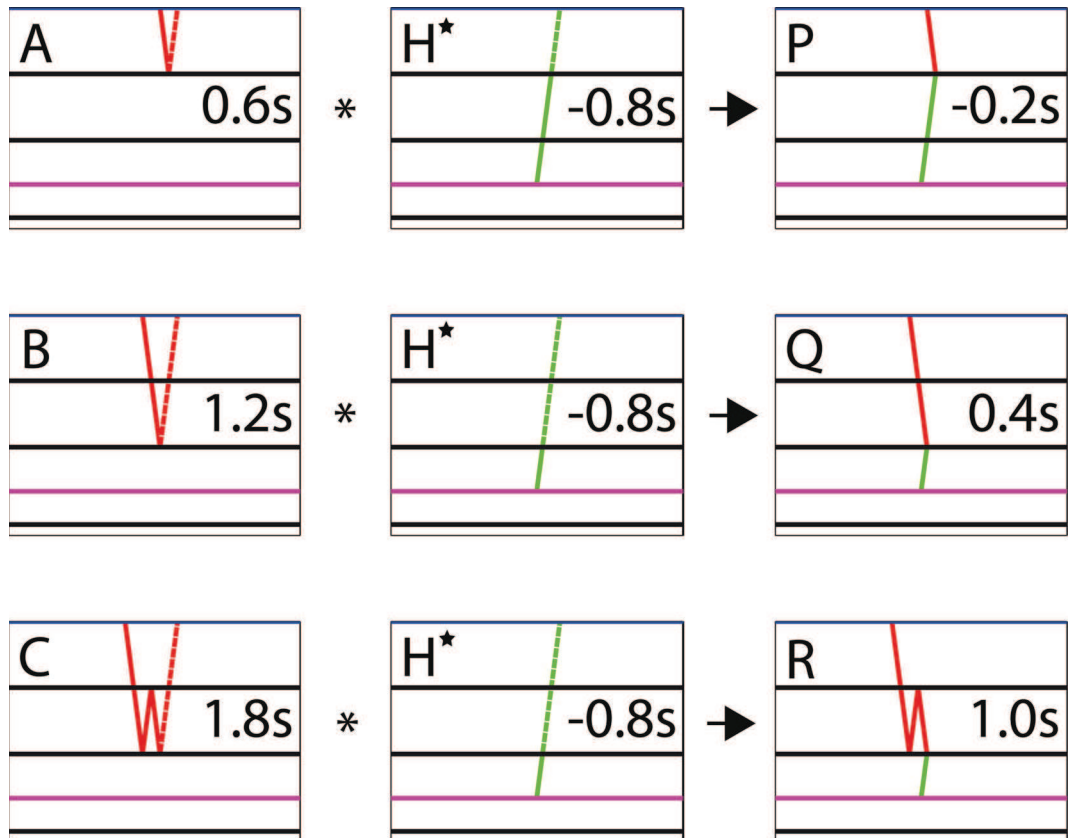


**Figure 5.** Illustrations of the retrieval of events P, Q and R. In each case, the time-reversed (indicated by superscript  $\star$ ) event  $H^\star$  is convolved with an event (A, B or C) in the reflection response. Traveltimes along red ray paths are positive, whereas traveltimes along green ray paths are negative. Hence, the traveltimes of events P, Q and R can be found by subtracting the traveltimes along the green ray paths from the traveltimes along the red ray paths (the numbers represent traveltimes at normal incidence). The dashed lines represent the parts of the ray paths that overlay and are subtracted.

The stacked gather  $\mathbf{Rf}_{1d}^+$  is shown in Fig. 4(b). The dashed green line indicates the trace that is obtained by stacking the correlation gather in Fig. 4(a). From eq. (16), we can learn that the constructed gather  $\mathbf{Rf}_{1d}^+$  can be interpreted as an initial estimate of the superposition of the upgoing focusing function  $f_1^-$  and the upgoing Green's function  $g^-$ . From eqs (19) and (28), we note that the estimate of  $g^-$  should be located outside the red curves (indicating where  $\Theta$  is applied), whereas the estimate of  $f_1^-$  should be located in between these curves. In between the curves, we find two events that we label as P and Q. The origin of these events is explained in the first two panels of Fig. 5. The traveltimes of these events are found by subtracting the traveltimes along the green ray paths from the trav-

eltimes along the red ray paths in the schematics. The traveltimes at normal incidence are indicated in the figure. We refer to these events as virtual events, using the terminology of Ikelle (2006), who also observed these artefacts of inverse wavefield extrapolation and reasoned how they may be used to predict internal multiples. However, our approach is different from that of Ikelle (2006), in the sense that we base our observations on the coupled Marchenko equations, where we do not have to identify these virtual events in practice, since they are separated automatically from the Green's functions by the actions of  $\Theta$  at each iteration. There are also virtual events outside the red curves in Fig. 4. A clear example is event R, whose origin is explained in the lowest panel of Fig. 5. This virtual event,

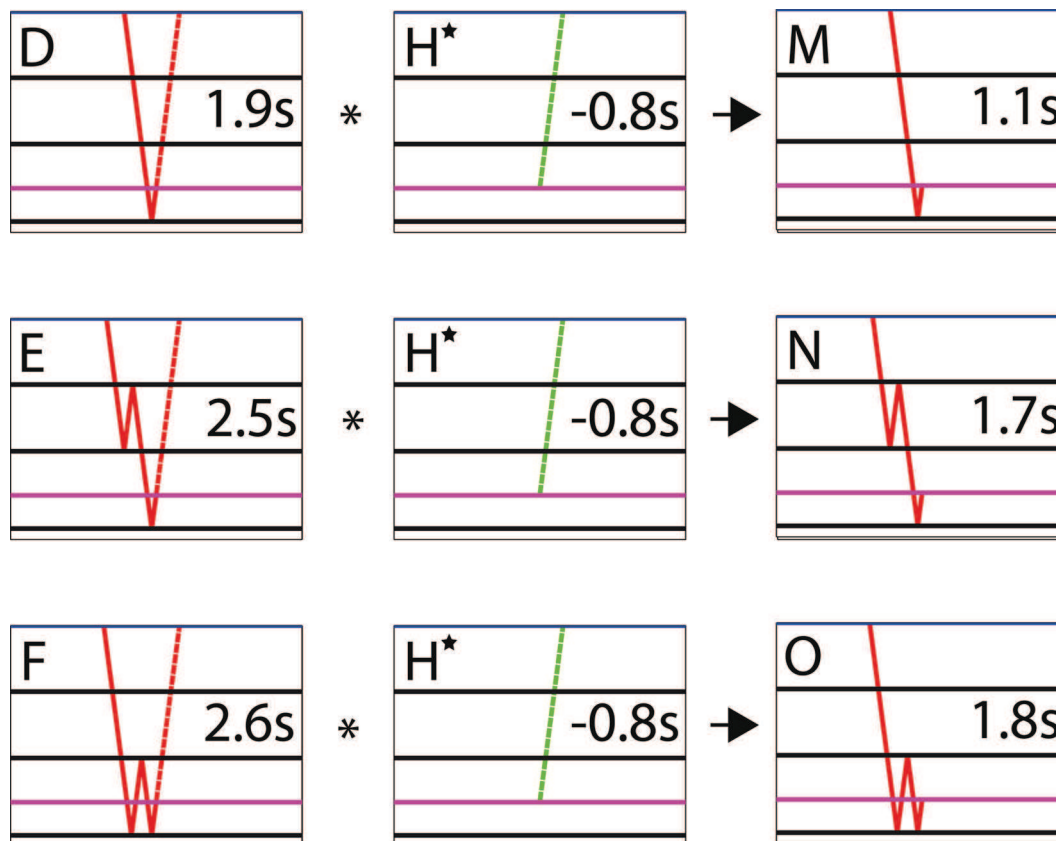


**Figure 6.** Illustrations of the retrieval of events M, N and O. In each case, the time-reversed event  $H^*$  is convolved with an event (D, E or F) in the reflection response. Note that M, N and O are all upgoing reflections with positive traveltimes.

stemming from the internal multiple C in the reflection data, appears after the direct wave and therefore could be mistaken for a deeper primary reflection. Hence, this type of event is prone to produce artefacts in seismic imaging (Malcolm *et al.* 2007), where inverse extrapolators like  $f_{1d}^+$  are generally used to reconstruct wavefields in the subsurface. Apart from the virtual events, we find the physical reflections of  $g^-$  outside the red curves. These are the events M, N and O that we also indicated in Fig. 3(b). Their retrieval is illustrated by the schematics in Fig. 6. Note that in the initial step of the iterative scheme, all upgoing primaries and internal multiples of the upgoing Green's function are retrieved. However, we also find virtual events. Later, we will see how the virtual events in between the red curves are utilized to eliminate the virtual events outside the curves, allowing us to retrieve  $g^-$  without artefacts. Moreover, we will see how the polarity- and time-reversed downgoing Green's function  $-g^{+*}$  is constructed.

### 4.3 Step 2: updating the downgoing wavefields

In the second step of the iterative scheme, the initial estimate of  $f_1^-$  that follows from eq. (29) (containing only the events P and Q) is propagated backward in time with the reflection response, following eq. (30). A correlation gather and a stacked gather for this operation are shown in Fig. 7. Once more, we have drawn the red curves that define the muting times for window matrix  $\Theta$ . The gather in Fig. 7(b) can be interpreted as an initial estimate of the sum of the two terms on the left-hand side of eq. (18). The time- and polarity-reversed downgoing Green's function  $-g^{+*}$  is located outside the red curves, as is the initial focusing function

$f_{1d}^+$ . The coda of the focusing function  $f_{1m}^+$  is situated in between the curves. Note from Fig. 7 that we find only one event S in between the curves, whose origin is explained in the upper panel of Fig. 8. This event is a vital ingredient for removing the artefacts that were observed in the upgoing Green's function (e.g. event R), as we will see later. Outside the curves, we find updates of event  $H^*$  (where superscript  $*$  denotes that it is time-reversed), which is the time-reversed direct wave that initiated the scheme. Explanations are given in the lowest two panels of Fig. 8. These updates are important to retrieve the exact amplitude of the Green's function. However, it should be noted that exact amplitudes can only be retrieved when the iterative scheme is initiated with the inverse of the direct wavefield in the true medium (Wapenaar *et al.* 2014a). In practice, the initial focusing function is generally computed in a smooth background model. As a consequence, the retrieved Green's functions are scaled versions of the exact Green's functions. We also find events  $I^*$ ,  $J^*$ ,  $K^*$  and  $L^*$  in Fig. 7. Their origins are explained in Fig. 9 (the schematic for event  $K^*$  is omitted, but its explanation is similar to the others). Note that these are all time-reversed internal multiples of the downgoing wavefield that can also be found in Fig. 3(a). The polarity of these events is reversed compared to that in Fig. 3(a), as we expect from the minus sign in the first term of eq. (18). Note that all major downgoing internal multiples are already visible in this first estimate of  $-g^{+*}$ , with relatively accurate amplitudes. These events are constructed by crosscorrelating two primary reflections and the direct wavefield. This mechanism is closely related to that of various other schemes that predict internal multiples at the surface by crosscorrelation of three primary reflections (Weglein *et al.* 1997; Jakubowicz 1998; Ten Kroode 2002; Ikelle 2006). This analogy has

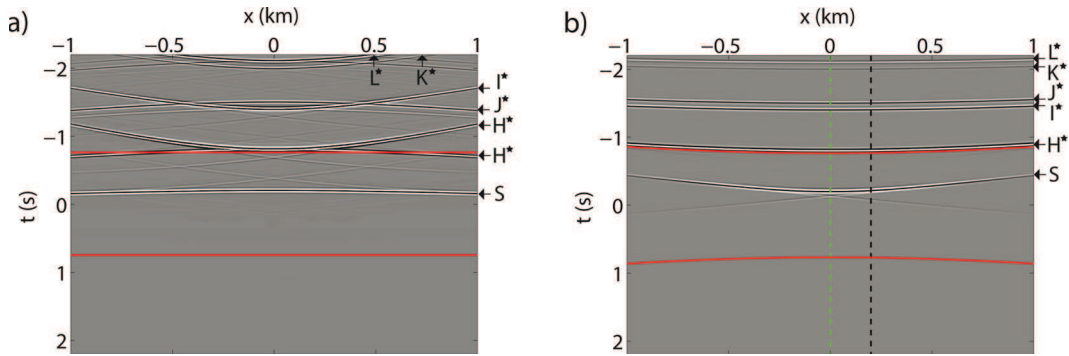


**Figure 7.** (a) Correlation gather of  $\mathbf{R}^* \mathbf{f}_1^-$  with  $\chi_B$  and  $\chi_F$  both at  $x = 0$  km. (b) Gather of  $\mathbf{R}^* \mathbf{f}_1^-$  with  $\chi_F$  at  $x = 0$  km. The traces at the dashed green and black lines are constructed by stacking the gathers in panel (a) and Fig. 13(b), respectively. The red curves define the muting times for matrix  $\Theta$ .

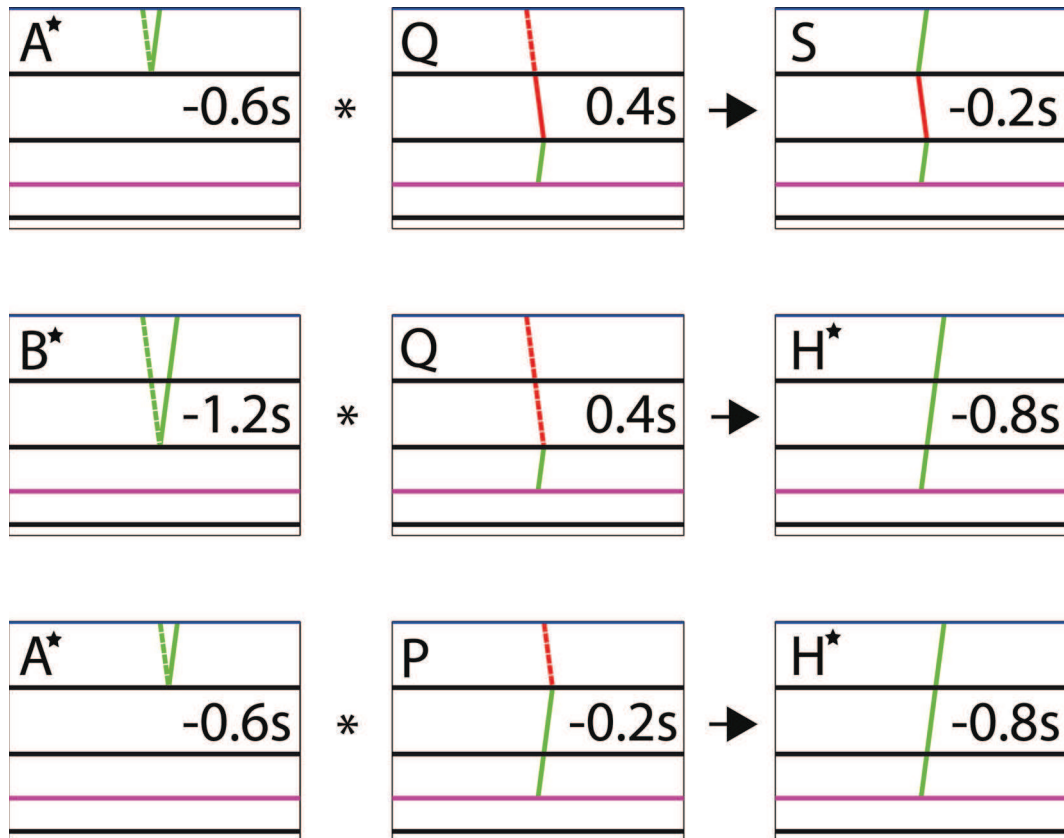


**Figure 8.** Illustrations of the retrieval of events S and  $H^*$ . In each case, an event of  $\mathbf{f}_1^-$  (Q or P) is convolved with a time-reversed event ( $A^*$  or  $B^*$ ) in the reflection response.

also been mentioned by Sheiman (private communication, 2014). During higher-order iterations, the amplitudes of the events are updated, as illustrated by Wapenaar *et al.* (2014a), Brogini *et al.* (2014b) and Slob *et al.* (2014).

#### 4.4 Step 3: updating the outgoing wavefields

To facilitate the third step of the iterative scheme, an estimate of  $\mathbf{f}_{1m}^+$  is obtained by muting all information outside the red curves in the retrieved gather of  $\mathbf{R}^* \mathbf{f}_1^-$  (see eq. 30). This estimate is propagated forward in time with the reflection response, yielding  $\mathbf{R} \mathbf{f}_{1m}^+$ . When added to the result of  $\mathbf{R} \mathbf{f}_{1d}^+$ , we should find a new estimate of  $\mathbf{f}_1^-$  in between the red curves and a new estimate of  $\mathbf{g}^-$  outside these

curves, as can be learned from eq. (16). In Fig. 10 (showing a correlation gather and a stacked gather of  $\mathbf{R} \mathbf{f}_{1m}^+$ ), we observe a single event in between the curves. From the schematic in the upper panel of Fig. 11, we can learn that this event has similar kinematics as event Q that appeared in the previous figures (e.g. in Fig. 5). Hence, the amplitude of this event is updated. Outside the red curves, we find various other events. First, we note event R that also appeared in Fig. 5. Note that this event is not part of the outgoing Green's function and therefore should be removed from the initial estimate of  $\mathbf{g}^-$  that we found in the first iteration. However, since the polarity of event R is reversed in  $\mathbf{R} \mathbf{f}_{1m}^+$  with respect to  $\mathbf{R} \mathbf{f}_{1d}^+$  (compare Figs 10b and 4b), this artefact is indeed suppressed when both terms are added together.

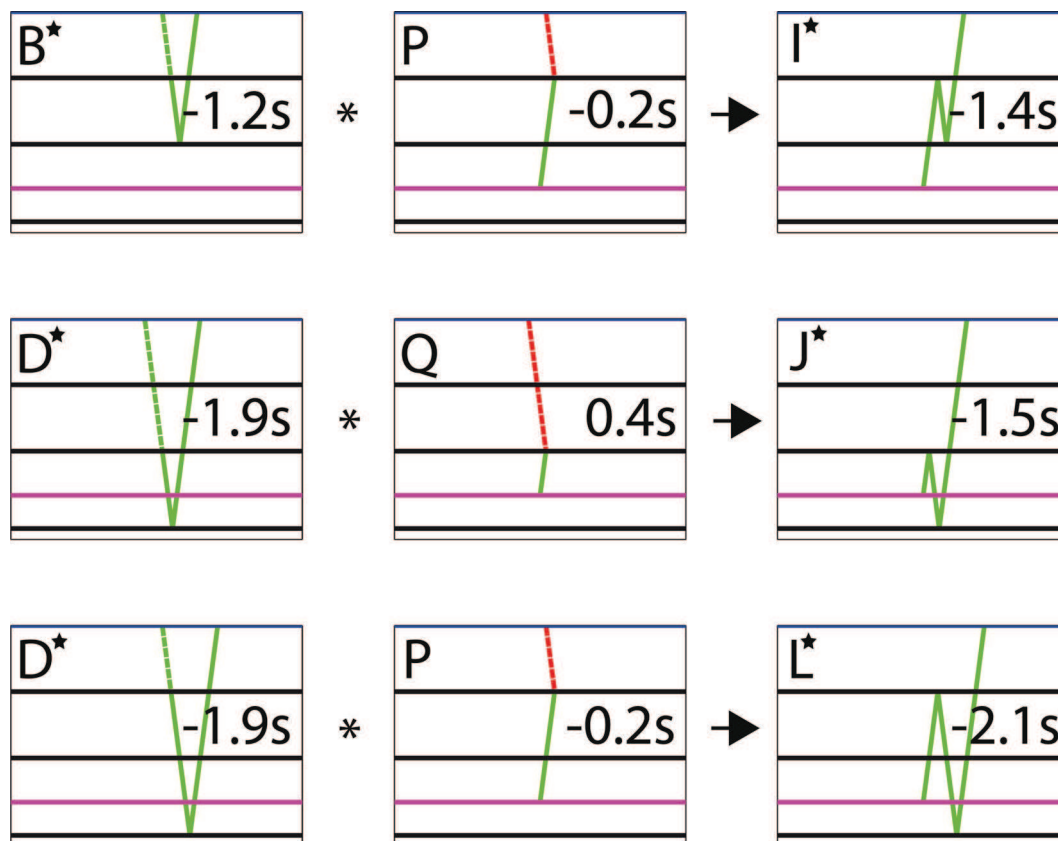


**Figure 9.** Illustrations of the retrieval of events  $I^*$ ,  $J^*$  and  $L^*$ . In each case, an event of  $f_1^-$  (P or Q) is convolved with a time-reversed event ( $B^*$  or  $D^*$ ) in the reflection response. Note that  $I^*$ ,  $J^*$  and  $L^*$  are all time-reversed downgoing reflections with negative traveltimes.

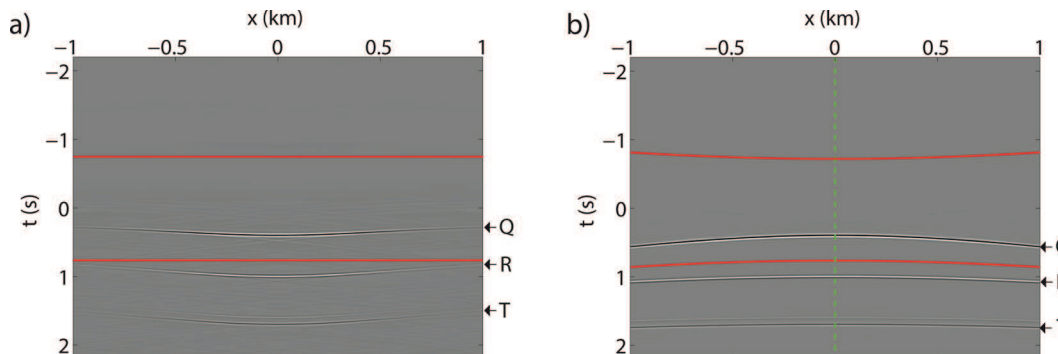


**Figure 10.** (a) Correlation gather of  $Rf_{1m}^+$  with  $\chi_B$  and  $\chi_F$  both at  $x = 0$  km. (b) Gather of  $Rf_{1m}^+$  with  $\chi_F$  at  $x = 0$  km. The trace at the dashed green line is constructed by stacking the gather in panel (a). The red curves define the muting times for matrix  $\Theta$ .

### 4.5 Green's function estimates

After three iterations of the scheme, we can already retrieve a reasonable estimate of the Green's function. To illustrate this, we compute the upgoing and downgoing Green's functions with eqs (34) and (35), using the obtained (first-order) estimates of  $f_1^-$  and  $f_{1m}^+$ . The retrieved gathers are shown in Fig. 12. Note that these results are already quite accurate with respect to the directly modelled Green's functions that we showed in Fig. 3. We can also confirm that event R that appeared in Fig. 4 has been significantly suppressed by including the update from  $Rf_{1m}^+$ , although some remnants remain. On a similar note, event T (explained by the schematic in the lowest panel of Fig. 11) eliminates an artefact that appears after the first step of the iterative scheme. However, this event cannot be identified in Fig. 4, since its arrival time coincides with that of event N.

The result can be improved by including higher-order iterations (Wapenaar *et al.* 2014a). Alternatively, the updates can be summed adaptively, as illustrated by Van der Neut *et al.* (2015a).

### 4.6 Stationary points

Whether a particular event can be retrieved at a particular offset depends on the acquisition design. As in seismic interferometry, particular stationary points exist that should be sampled (Schuster 2009). In Fig. 4(a), we showed the correlation gather for a trace between surface location  $\chi_B$  and focal point  $\chi_F$ , both chosen at  $x = 0$  km. Since there is no (horizontal) offset between  $\chi_B$  and  $\chi_F$  in this case and the layers are flat, all stationary points are found at  $x = 0$  km. However, when  $\chi_B$  is chosen at an offset from  $\chi_F$ ,

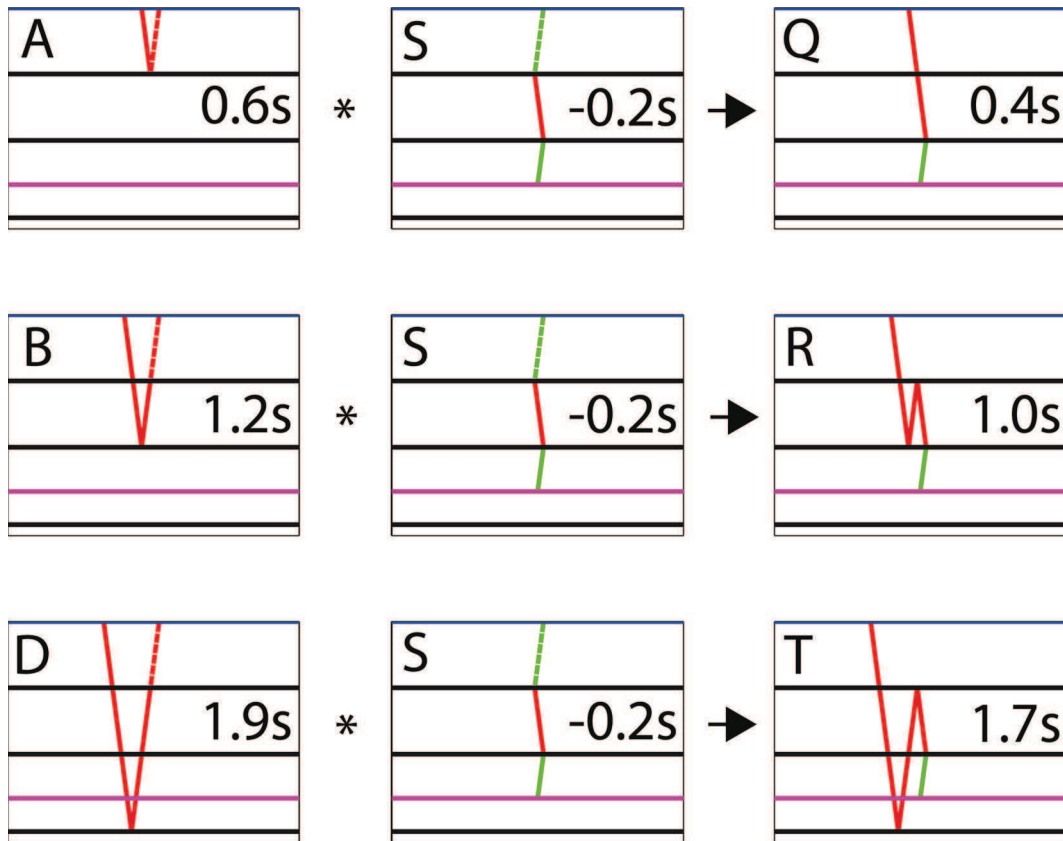


Figure 11. Illustrations of the retrieval of events Q, R and T. In each case, event S is convolved with an event (A, B or D) in the reflection response.

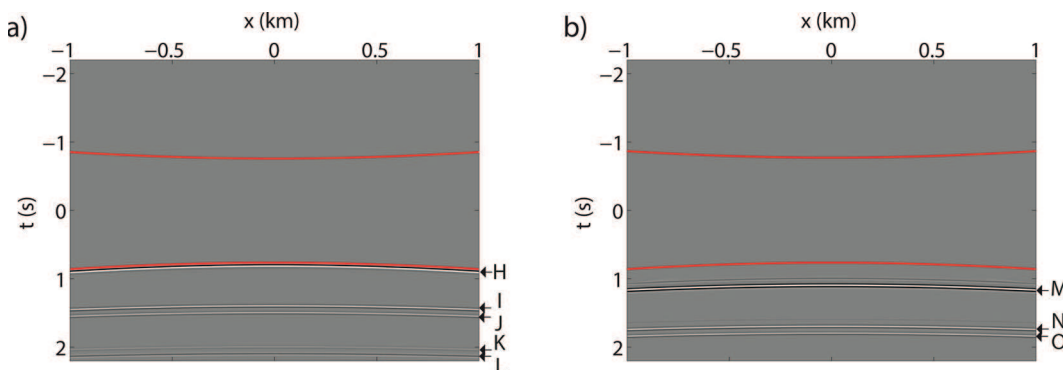


Figure 12. (a) Estimate of the downgoing Green's function obtained by eq. (35), using the first-order estimate of  $f_1^-$ . (b) Estimate of the upgoing Green's function obtained by eq. (34), using the first-order estimate of  $f_{1m}^+$ .

the situation is different. As an example, we take  $\chi_B$  at  $x = 0.2$  km and  $\chi_F$  at  $x = 0$  km, yielding the correlation gather in Fig. 13(a). It is clear that the stationary points are shifted. The stationary point of event M (a primary reflection), for example, is found at  $x \approx -0.145$  km. This location can easily be confirmed, since the ray paths of the reflected event D and the time-reversed direct wave  $H^*$  that construct event M (see the upper panel in Fig. 6) overlay each other at this location. Similar reasoning can be applied to find the stationary points of the virtual events P and Q. In Fig. 14, we show how the stationary points of these events are found at  $x = 0.8$  km and  $x = -0.4$  km, confirming the observations in Fig. 13(a). Note from the schematics that the rays with positive and negative traveltimes bend in opposite directions. This phenomenon has been referred to by Ikelle & Gangi (2007) as negative ray bending. The construction is relatively simple in this medium, since the layers are flat and

the velocity is constant. However, a similar analysis could also be done in media with velocity variations and curved interfaces. The stationary points of other events can also be constructed. In Fig. 13(b), for instance, we show the correlation gather for the second step of the iterative scheme,  $R^*f_1^-$  with  $\chi_B$  at  $x = 0.2$  km and  $\chi_F$  at  $x = 0$  km. The stationary points of events S and  $I^*$  are located at  $x = -0.4$  km and  $x = 0.04$  km, respectively. In Fig. 15, we also confirm the locations of these stationary points graphically.

### 5 POINT SCATTERERS EXAMPLE

It should be well understood that exact Green's function retrieval by iterative substitution of the coupled Marchenko equations is only possible if the assumptions that are made in the underlying

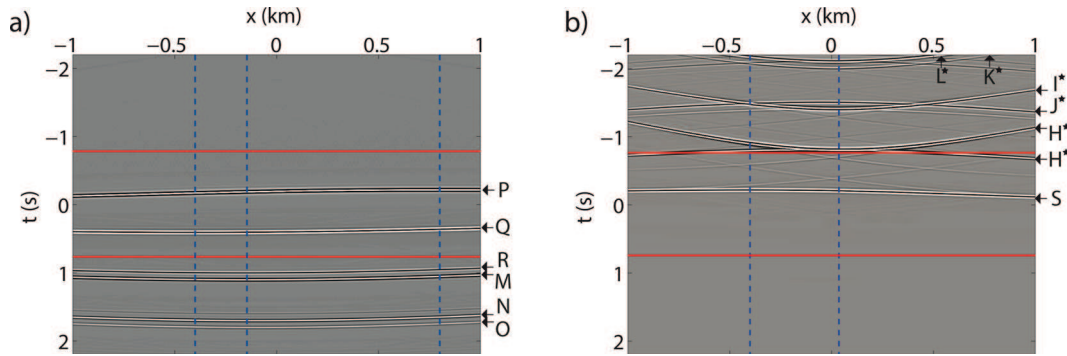


**Figure 13.** (a) Correlation gather of  $Rf_{1d}^+$  with  $x_B$  at  $x = 0.2$  km and  $x_F$  at  $x = 0$  km. The blue dashed lines indicate the stationary points of events Q (at  $x = -0.4$  km), M (at  $x \approx -0.145$  km) and P (at  $x = 0.8$  km). (b) Correlation gather of  $R^*f_1^-$  with  $x_B$  at  $x = 0.2$  km and  $x_F$  at  $x = 0$  km. The blue dashed lines indicate the stationary points of events S (at  $x = -0.4$  km) and  $I^*$  (at  $x = 0.04$  km).

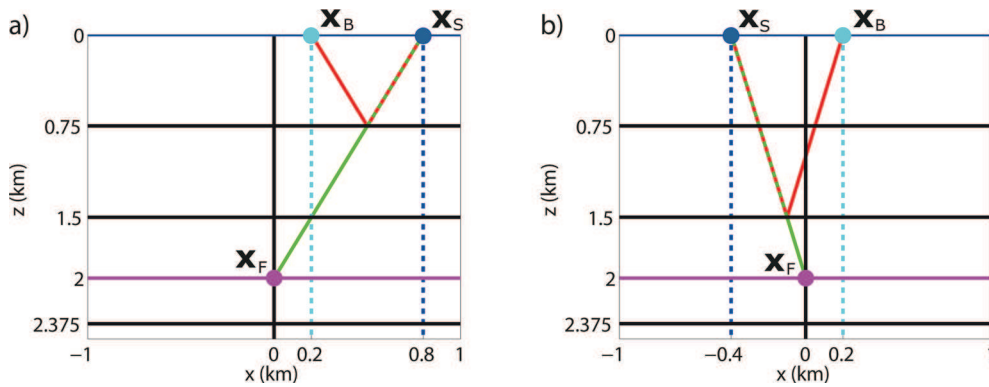


**Figure 14.** Illustration of the construction of events (a) P (from events A and  $H^*$  as shown in the upper panel of Fig. 5) and (b) Q (from events B and  $H^*$  as shown in the middle panel of Fig. 5) with  $x_B$  (cyan dot) at  $x = 0.2$  km and  $x_F$  (magenta dot) at  $x = 0$  km. From these illustrations, it is confirmed that the stationary points  $x_S$  (blue dots) of events P and Q are located at  $x = 0.8$  km and  $x = -0.4$  km, respectively. At these stationary points, the red and green ray paths overlay and cancel.

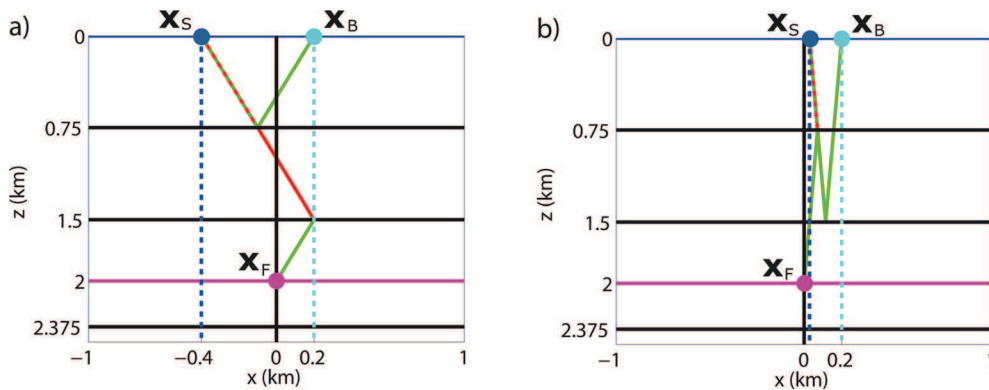


**Figure 15.** Illustration of the construction of events (a) S (from events  $A^*$  and Q as shown in the upper panel of Fig. 8) and (b)  $I^*$  (from events  $B^*$  and P as shown in the upper panel of Fig. 9) with  $x_B$  (cyan dot) at  $x = 0.2$  km and  $x_F$  (magenta dot) at  $x = 0$  km. From these illustrations, it is confirmed that the stationary points  $x_S$  (blue dots) of events S and  $I^*$  are located at  $x = -0.4$  km and  $x = 0.04$  km, respectively. At these stationary points, the red and green ray paths overlay and cancel.

derivation are fulfilled. The most important assumption is that the desired Green's function should consist of a direct wave with a distinct arrival time that does not interfere with its coda. From a theoretical point of view, any forward-scattered event (which we define as scattering in which the vertical propagation direction is not altered) should be included in the initial estimate of the focusing function (Wapenaar *et al.* 2014b), but even then the consequences of having more than a single event in  $f_{1d}^+$  need further investigation. In this section, we analyse the performance

of the iterative scheme in a medium with point scatterers. Even though we do not include forward scattering in the initial focusing function, we show that the scheme still works reasonably well in such a medium, which we explain in terms of the interferometric interpretation that we have developed in the previous section. Once again, each step of the scheme will be evaluated individually. In the end, we will expose some of the consequences of not obeying the assumptions that undergird the coupled Marchenko equations.

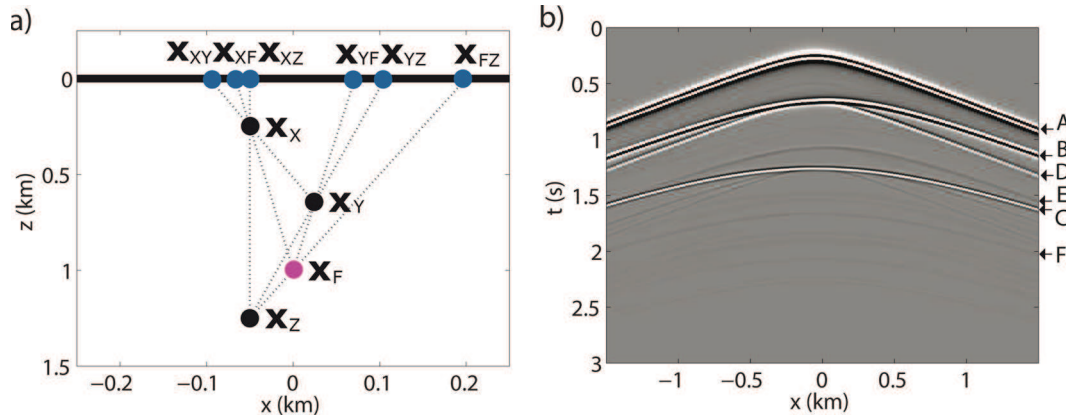


**Figure 16.** (a) Synthetic 2-D model with three point scatterers (located at  $\mathbf{x}_X$ ,  $\mathbf{x}_Y$  and  $\mathbf{x}_Z$ ) in a homogeneous background with velocity  $c = 2 \text{ km s}^{-1}$  and density  $\rho = 1000 \text{ kg m}^{-3}$ . The black solid line denotes the acquisition surface and the magenta dot is the focal point  $\mathbf{x}_F$ . We have also indicated the location of various stationary points (blue dots). (b) Reflection response with a source at  $x = 0 \text{ km}$  at the acquisition level. Various events are labelled.

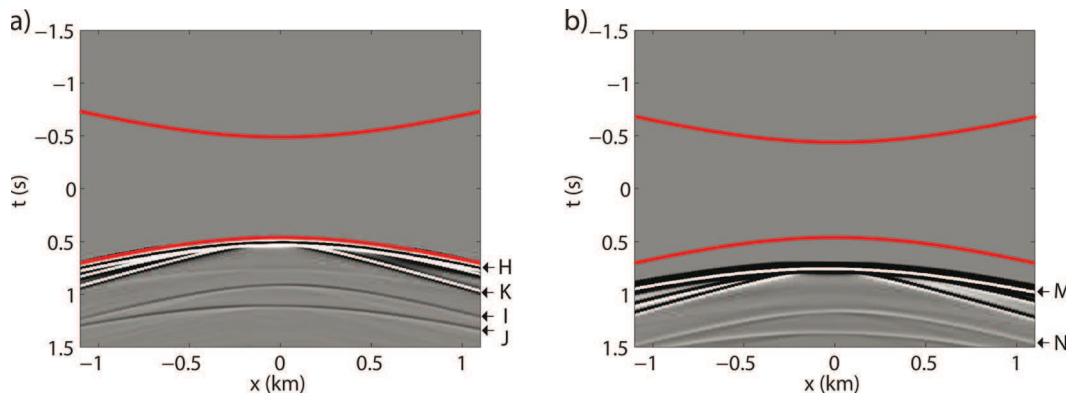


**Figure 17.** (a) Downgoing Green's function. (b) Upgoing Green's function. Both gathers are common receiver gathers that have been obtained by direct modelling and wavefield decomposition. Sources are located at the acquisition level and a single receiver is deployed at  $x = 0 \text{ km}$  at the focusing level. The red curves define the muting times for matrix  $\Theta$ .

### 5.1 The model

In Fig. 16(a), we show a 2-D synthetic model with three point scatterers at locations  $\mathbf{x}_X$ ,  $\mathbf{x}_Y$  and  $\mathbf{x}_Z$ . These scatterers are embedded in a homogeneous background with a velocity of  $2 \text{ km s}^{-1}$ . At the acquisition surface, a fixed grid with 801 sources and 801 receivers is deployed with source and receiver spacing  $\Delta x = 5 \text{ m}$ . The focal point  $\mathbf{x}_F$  is chosen at  $1 \text{ km}$  depth. We have indicated various stationary points that will show up in the analysis to come:  $\mathbf{x}_{XY}$ ,  $\mathbf{x}_{XF}$ ,  $\mathbf{x}_{XZ}$ ,  $\mathbf{x}_{YF}$ ,  $\mathbf{x}_{YZ}$  and  $\mathbf{x}_{FZ}$ . These stationary points are found by intersecting the acquisition surface with lines that connect in pairs the individual locations  $\mathbf{x}_X$ ,  $\mathbf{x}_Y$ ,  $\mathbf{x}_Z$  and  $\mathbf{x}_F$ , where we used the fact that the propagation velocity is constant. In Fig. 16(b), we show a shot record where the source is located at  $x = 0 \text{ m}$ . The desired downgoing and upgoing Green's functions are shown in Fig. 17, for reference. These responses have been obtained with a modelling code of Galetti *et al.* (2013) and wavefield decomposition (Wapenaar & Grimbergen 1996). The red curves define the muting times for matrix  $\Theta$ .

### 5.2 Step 1: initiating the upgoing wavefields

The direct wave from the acquisition surface to the focal point is computed in a homogeneous background medium without point scatterers. The initial focusing function is obtained by time-reversing this direct wave. The iterative scheme is initiated by prop-

agating this initial focusing function forward in time with the reflection response, following eq. (29) (with the initial estimate  $\mathbf{f}_{1m}^+ = \mathbf{0}$ ). In Fig. 18(b), we show the result of this operation,  $\mathbf{R}\mathbf{f}_{1d}^+$ , where each trace is obtained by stacking a correlation gather. As an example, one such correlation gather is shown in Fig. 18(a). The red curves indicate the muting times that are needed for matrix  $\Theta$ . Several events have been labelled. In between the red curves, we find events P, Q and U. In Fig. 19, we illustrate how events P and U are constructed (a similar schematic could be made for event Q). From these schematics, we can learn that the stationary points to retrieve these events are located at  $\mathbf{x}_{XF}$  (for event P) and  $\mathbf{x}_{YF}$  (for event U). It can be confirmed in the correlation gathers in Fig. 18(a) that events P and U are indeed stationary at these locations. Since these events are in between the red curves, they represent our initial estimate of  $\mathbf{f}_1^-$  (see eq. 29). Outside the curves, we find events M, N, R and T. As an illustration, we have visualized the construction of events M and R in Fig. 19. The stationary points for these events are located at  $\mathbf{x}_{FZ}$  (for event M) and  $\mathbf{x}_{YF}$  (for event R). Once more, these locations can be confirmed in the correlation gather in Fig. 18(a). Since these events are located outside the red curves, they represent our initial estimate of  $\mathbf{g}^-$  (see eq. 16). By comparing Figs 18(b) and 17(b), it is indeed clear that events M and N are physical upgoing reflections that have been retrieved correctly. We also observe several unlabelled events that branch off from event M. These waveforms have forward-scattered at  $\mathbf{x}_X$  and  $\mathbf{x}_Y$  before scattering at  $\mathbf{x}_Z$ . Deeper in the gather, we find two internal multiples. Special attention should be

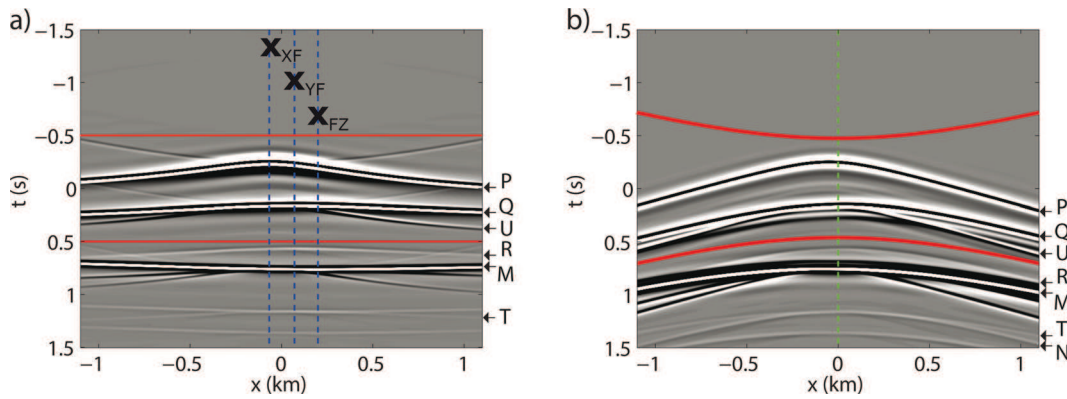


**Figure 18.** (a) Correlation gather of  $\mathbf{Rf}_{ld}^+$  with  $\mathbf{x}_B$  and  $\mathbf{x}_F$  both at  $x = 0$  km. (b) Gather of  $\mathbf{Rf}_{ld}^+$  with  $\mathbf{x}_F$  at  $x = 0$  km. The trace at the dashed green line is constructed by stacking the gather in panel (a). The dashed blue lines indicate the stationary phase points  $\mathbf{x}_{XF}$ ,  $\mathbf{x}_{YF}$  and  $\mathbf{x}_{FZ}$  that can also be found in Fig. 16(a). The red curves define the muting times for matrix  $\Theta$ .

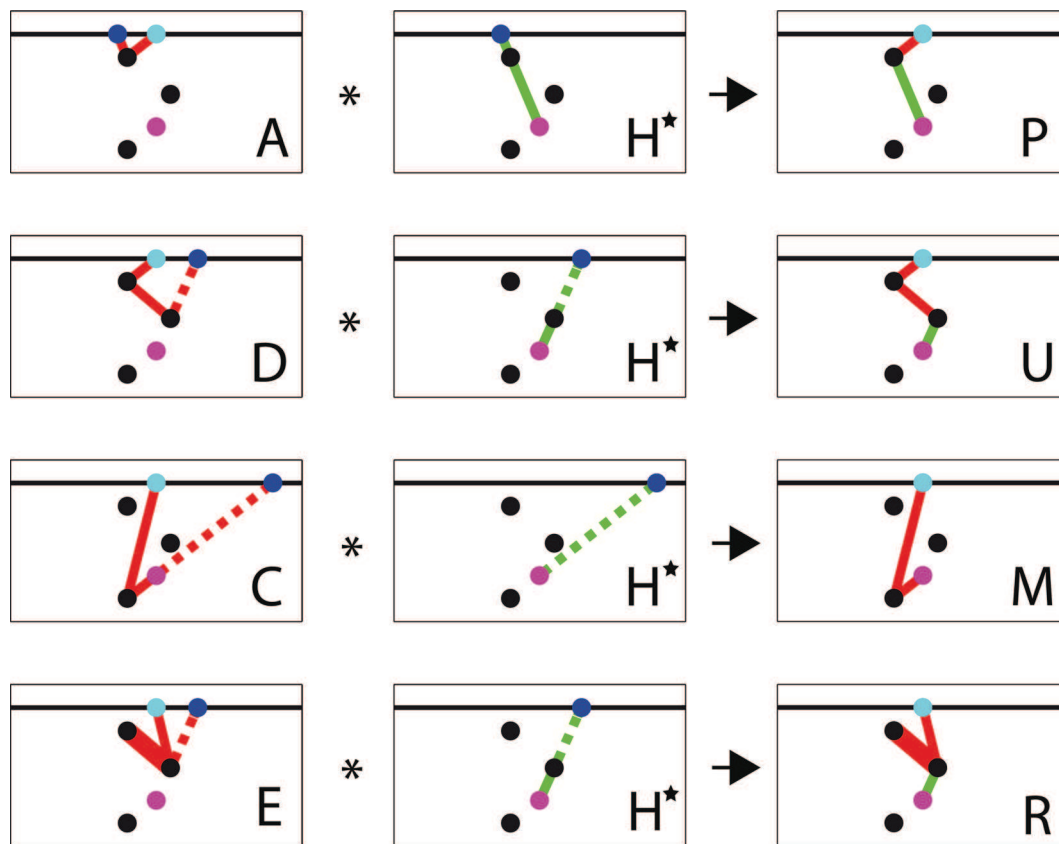


**Figure 19.** Illustrations of the retrieval of events P, U, M and R. In each case, the time-reversed (indicated by superscript  $\star$ ) event  $H^\star$  is convolved with an event (A, D, C or E) in the reflection response. Events P and U are part of the focusing function. Event M is a physical upgoing reflection, while event R is an artefact. Traveltimes along red ray paths are positive, whereas traveltimes along green ray paths are negative. The dashed lines represent the parts of the ray paths that overlay and are subtracted. The thick red lines (in events R and E) indicate that the path has been traversed twice. The dark blue dots indicate stationary points at the surface.

paid to events R and T. These are artefacts that should be suppressed during higher-order iterations, as we will show in the following.

### 5.3 Step 2: updating the downgoing wavefields

The window matrix  $\Theta$  is designed such that all data outside the red curves in Fig. 18(b) are muted. The resulting estimate,  $\mathbf{f}_1^- = \Theta \mathbf{Rf}_{ld}^+$  (containing events P, Q and U, but not R, M, T and N), is propagated backward in time with the reflection response, following

eq. (30). In Fig. 20, we show a correlation gather and the retrieved gather of this operation,  $\mathbf{R}^* \mathbf{f}_1^-$ . In between the red curves, we find only event S, whose origin is explained in Fig. 21. The stationary point of this event is located at  $\mathbf{x}_{YY}$ . In the correlation gather in Fig. 20(a), we find that event S is indeed stationary at this location. Since S is the only event that is located in between the red curves, it represents our estimate of  $\mathbf{f}_{1m}^+$ . Outside the red curves, several events are situated, of which events  $K^*$ ,  $I^*$  and  $J^*$  have been labelled. Their origin is explained in Fig. 21. From these schematics, we

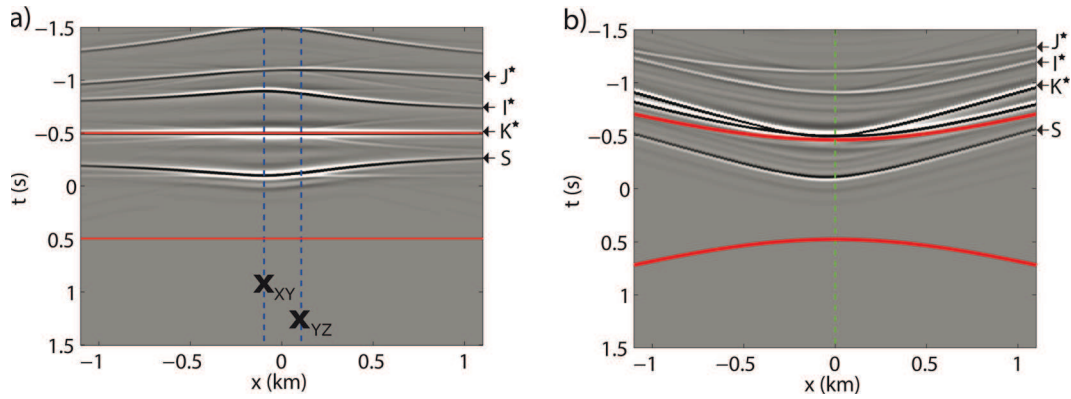


**Figure 20.** (a) Correlation gather of  $\mathbf{R}^* \mathbf{f}_1^-$  with  $\mathbf{x}_B$  and  $\mathbf{x}_F$  both at  $x = 0$  km. (b) Gather of  $\mathbf{R}^* \mathbf{f}_1^-$  with  $\mathbf{x}_F$  at  $x = 0$  km. The trace at the dashed green line is constructed by stacking the gather in panel (a). The dashed blue lines indicate the stationary points  $\mathbf{x}_{XY}$  and  $\mathbf{x}_{YZ}$  that can also be found in Fig. 16(a). The red curves define the muting times for matrix  $\Theta$ .

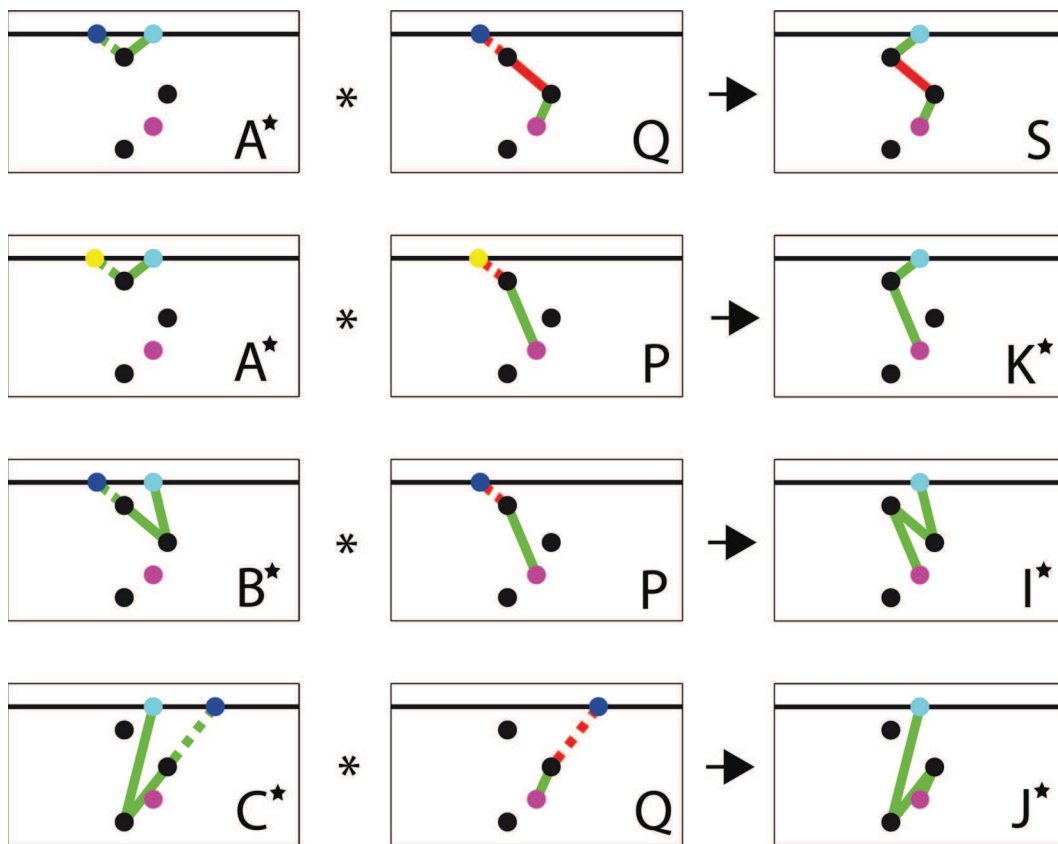


**Figure 21.** Illustrations of the retrieval of events  $S$ ,  $K^*$ ,  $I^*$  and  $J^*$ . In each case, an event ( $Q$  or  $P$ ) of  $\mathbf{f}_1^-$  is convolved with a time-reversed event ( $A^*$ ,  $B^*$  or  $C^*$ ) in the reflection response. Event  $S$  is part of the focusing function. Events  $K^*$ ,  $I^*$  and  $J^*$  are physical (time-reversed) downgoing reflections. The dark blue dots indicate stationary points at the surface. The yellow dots are arbitrary, since all locations at the surface are stationary.

learn that the stationary points of events  $I^*$  and  $J^*$  are found at  $\mathbf{x}_{XY}$  and  $\mathbf{x}_{YZ}$ , respectively. From the correlation gather in Fig. 20(a), it follows that these events are indeed stationary at these locations. For event  $K^*$ , however, every point is stationary, as is clear from the schematic in Fig. 21. Hence, event  $K^*$  is flat in the correlation gather, as can be observed in Fig. 20(a). Consequently, we require contributions along the entire surface to retrieve the exact amplitude of this event, posing limitations in practical cases with a finite recording aperture. This effect is also observed in Green’s function retrieval by seismic interferometry (Wapenaar *et al.* 2010). It accounts for nonlinear scattering effects at a single point scatterer. If

we compare Fig. 20(b) with Fig. 17(a), we observe that all events  $K^*$ ,  $I^*$  and  $J^*$  are constituents of the downgoing Green’s function, retrieved with negative polarity and reversed in time. This confirms that we have retrieved an estimate of  $-\mathbf{g}^{+*}$ , as we expect from eq. (18).

### 5.4 Step 3: updating the upgoing wavefields

When the window matrix  $\Theta$  is applied to the retrieved gather  $\mathbf{R}^* \mathbf{f}_1^-$ , all data, except for event  $S$ , are muted, resulting in an estimate of  $\mathbf{f}_{1m}^+$  (see eq. 30). To interpret this estimate, we propagate it forward

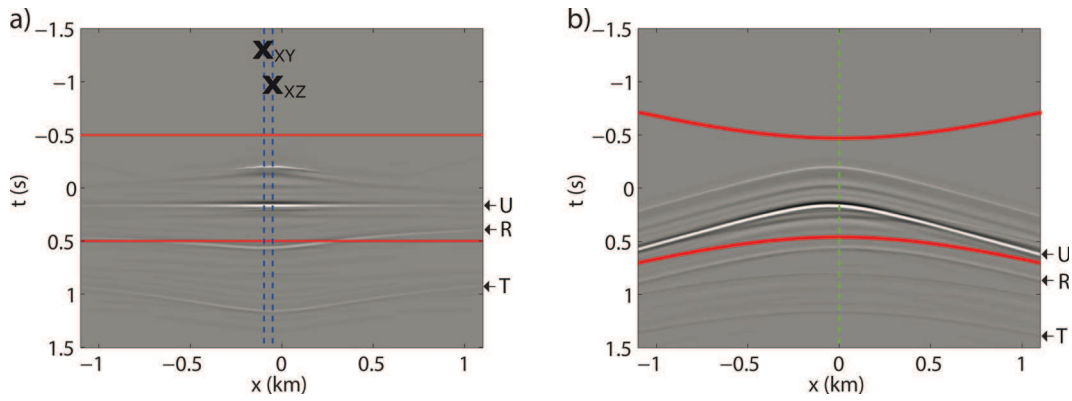


**Figure 22.** (a) Correlation gather of  $\mathbf{Rf}_{1m}^+$  with  $\mathbf{x}_B$  and  $\mathbf{x}_F$  both at  $x = 0$  km. (b) Gather of  $\mathbf{Rf}_{1m}^+$  with  $\mathbf{x}_F$  at  $x = 0$  km. The trace at the dashed green line is constructed by stacking the gather in panel (a). The dashed blue lines indicate the stationary phase points  $\mathbf{x}_{XY}$  and  $\mathbf{x}_{YZ}$  that can also be found in Fig. 16(a). The red curves define the muting times for matrix  $\Theta$ .

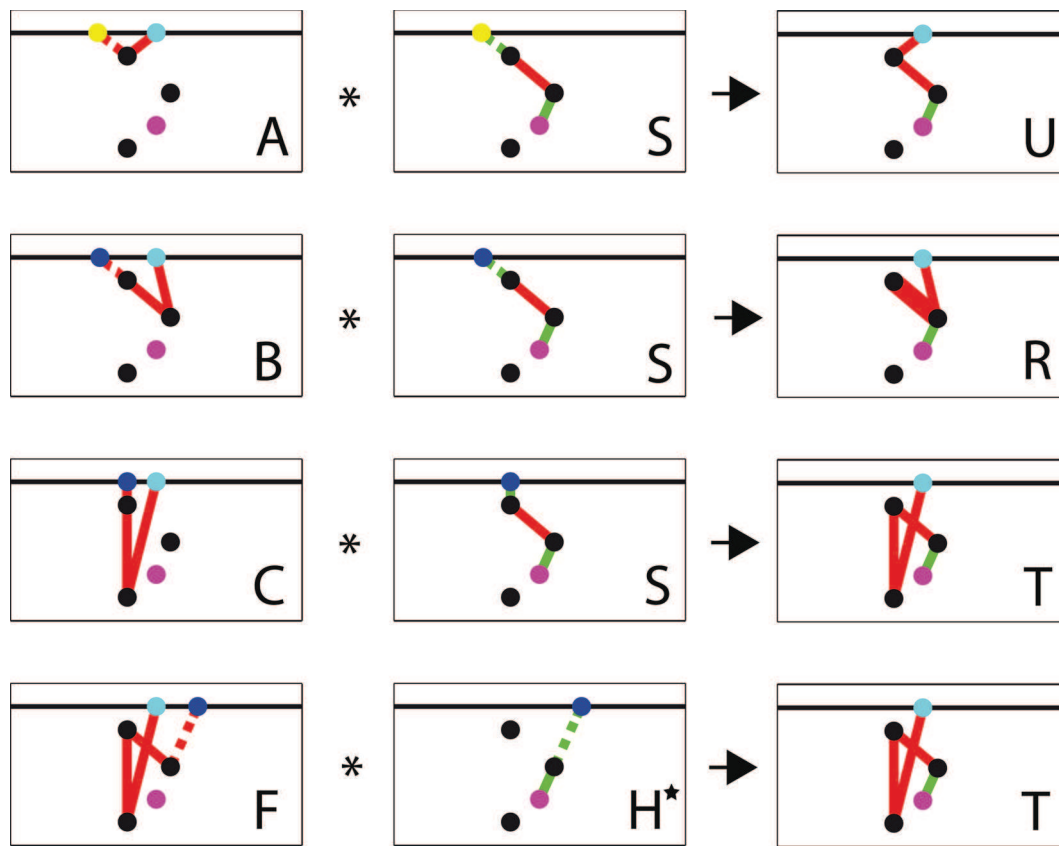


**Figure 23.** Illustrations of the retrieval of events U, R and T. In each case, event S of  $\mathbf{f}_{1m}^+$  is convolved with an event (A, B or C) in the reflection response. The lowest panels illustrate that event T also emerges in the first step of the iterative scheme, when event  $\mathbf{H}^*$  of  $\mathbf{f}_{1d}^+$  is convolved with event F in the reflection response. The dark blue dots indicate stationary points at the surface. The yellow dots are arbitrary, since all locations at the surface are stationary.

in time with the reflection response, as in  $\mathbf{Rf}_{1m}^+$ . The result of this operation is shown in Fig. 22. Once again, the red curves indicate the muting times that are needed for matrix  $\Theta$ . In between the curves, we find event U, whose origin is explained in the first panel of Fig. 23. Remember that a similar event U emerged in the first iteration, when  $\mathbf{Rf}_{1d}^+$  was evaluated (see Figs 18b and 19). Hence, the amplitude of this event is updated when  $\mathbf{f}_{1m}^+$  is added to the initial focusing function. Once more, it is observed that every location at the surface is stationary for the retrieval of event U. As a consequence, event U is flat in the correlation gather, as can be seen in Fig. 22(a). Hence, retrieving the exact amplitude of this event requires a very

large acquisition array at the surface. Outside the red curves, we find events R and T. Their construction is explained in the second and third panel of Fig. 23. Once more, we point out the necessity to sample stationary points  $\mathbf{x}_{XY}$  (for event R) and  $\mathbf{x}_{YZ}$  (for event T) to enable retrieval. These locations can be confirmed in the correlation gather in Fig. 22(a). Remember that event R was also retrieved in the first iteration, when  $\mathbf{Rf}_{1d}^+$  was evaluated (see Figs 18(b) and 19). However, as can be seen by comparing Figs 18(b) and 22(b), the predicted update has its polarity reversed. Hence, this artefact is suppressed when  $\mathbf{Rf}_{1d}^+$  and  $\mathbf{Rf}_{1m}^+$  are added. A similar reasoning holds for event T, which appears in the first iteration, as explained

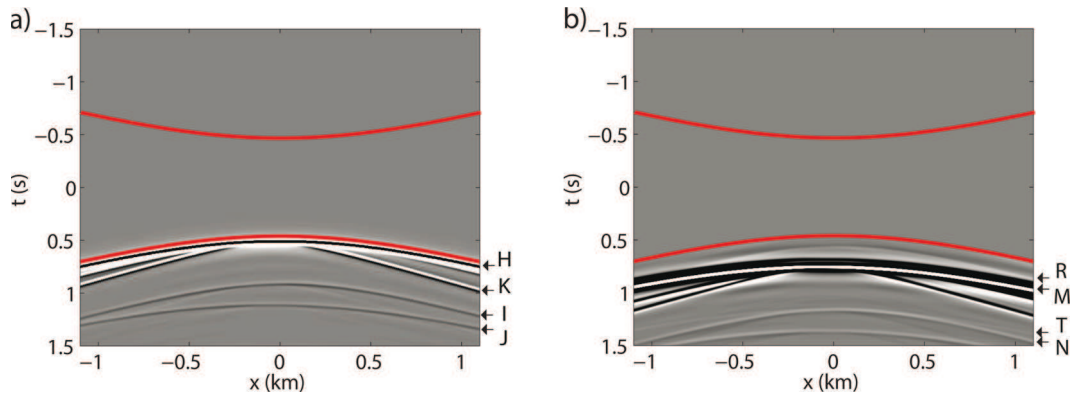


**Figure 24.** (a) Estimate of the downgoing Green's function obtained by eq. (35), using the first-order estimate of  $\mathbf{f}_1^-$ . (b) Estimate of the upgoing Green's function obtained by eq. (34), using the first-order estimate of  $\mathbf{f}_{1m}^+$ .

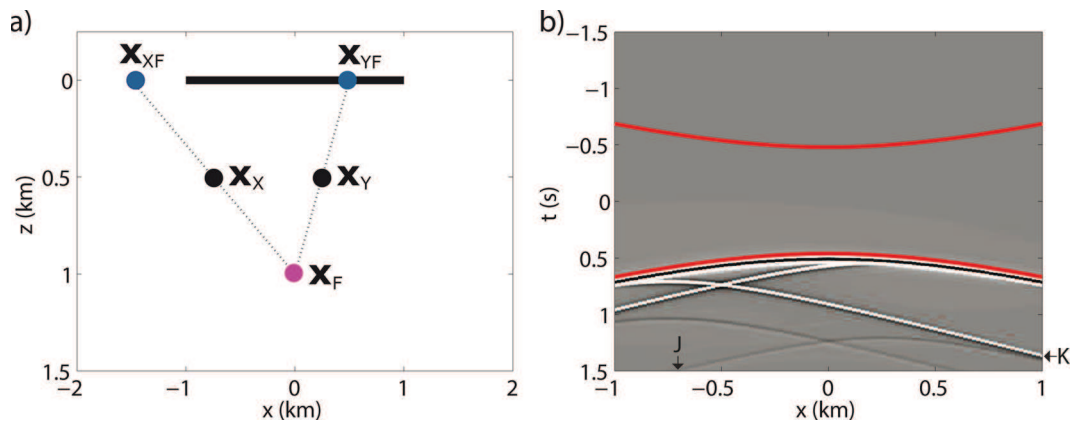


**Figure 25.** (a) Synthetic 2-D model with two point scatterers (located at  $\mathbf{x}_X$  and  $\mathbf{x}_Y$ ) in a homogeneous background with velocity  $c = 2 \text{ km s}^{-1}$  and density  $\rho = 1000 \text{ kg m}^{-3}$ . The acquisition array is indicated by the black solid line, covering  $[-1 \text{ km}, 1 \text{ km}]$ . We have also indicated the location of the focal point  $\mathbf{x}_F$  and stationary points  $\mathbf{x}_{XF}$  and  $\mathbf{x}_{YF}$ . Note that  $\mathbf{x}_{YF}$  is covered by the acquisition array but  $\mathbf{x}_{XF}$  is not. (b) Common receiver gather of the desired Green's function, obtained by direct modelling. Sources are located at the acquisition level and a single receiver is deployed at the focal point. Events K and J are indicated. The red curves define the muting times for matrix  $\Theta$ .

by the fourth panel of Fig. 23, and is updated by an event that we explain in the third panel of Fig. 23.

### 5.5 Green's function estimates

Finally, we can retrieve the upgoing and downgoing Green's functions with eqs (34) and (35). The results are shown in Fig. 24, where we used the retrieved (first-order) estimates of  $\mathbf{f}_1^-$  and  $\mathbf{f}_{1m}^+$ . Compared to the Green's functions in Fig. 17 that are obtained by direct modelling, we observe that all events such as H, K, I, J, M and N have been retrieved. Artefacts R and T are still visible in Fig. 24(b), but they are significantly weakened compared to Fig. 18(b) (which would be the retrieved upgoing field after a single iteration).

### 5.6 Limitations

As also mentioned by Wapenaar *et al.* (2014b), the causality conditions (eqs 27 and 28) that were used in the derivation of the coupled Marchenko equations are sufficient in media with moderately curved interfaces, but they are not generally true in arbitrary heterogeneous media. In fact, these conditions can easily be broken, even in relatively simple media with a few point scatterers. To illustrate this, we repeat the previous experiment with an alternative distribution of scatterers, see Fig. 25(a). The acquisition array contains 401

sources and 401 receivers (with source and receiver spacing  $\Delta x = 5 \text{ m}$ ) on the interval  $[-1 \text{ km}, 1 \text{ km}]$ . Note that stationary point  $\mathbf{x}_{YF}$  is covered by the acquisition array, but  $\mathbf{x}_{XF}$  is not. The large offset (1 km) between the point scatterers poses a complication, as will be illustrated. In Fig. 25(b), we show the wavefield when sources are excited at the surface and a receiver is positioned at the focal point. Our goal is to retrieve this wavefield by iterative substitution of the coupled Marchenko equations.

In Fig. 26(a), we show the result of the first step  $\mathbf{Rf}_{1d}^+$ , using data from this model. Events P and Q have been labelled. Their construction is explained in the upper two panels of Fig. 27. Since both scatterers are located at the same depth (0.5 km), we expect these events to be similar in terms of their amplitude and move-out. However, event P is significantly weaker and appears to be slightly mispositioned with respect to event Q. This mismatch can easily be explained from the fact that stationary point  $\mathbf{x}_{XF}$ , which is needed for the construction of event P, has not been sampled, as can also be seen in Fig. 27. Because of the finite acquisition array, we have truncated the integral that is evaluated by  $\mathbf{Rf}_{1d}^+$  and what has been labelled as event P in Fig. 26(a) is merely an artefact from this truncation. Similar artefacts are also known in seismic interferometry and have been well described in the literature (Mehta *et al.* 2008). To reduce such artefacts, the acquisition array can be tapered, but event P will be lost. On the contrary, event Q can still be retrieved well, since  $\mathbf{x}_{YF}$  is covered by the acquisition array.

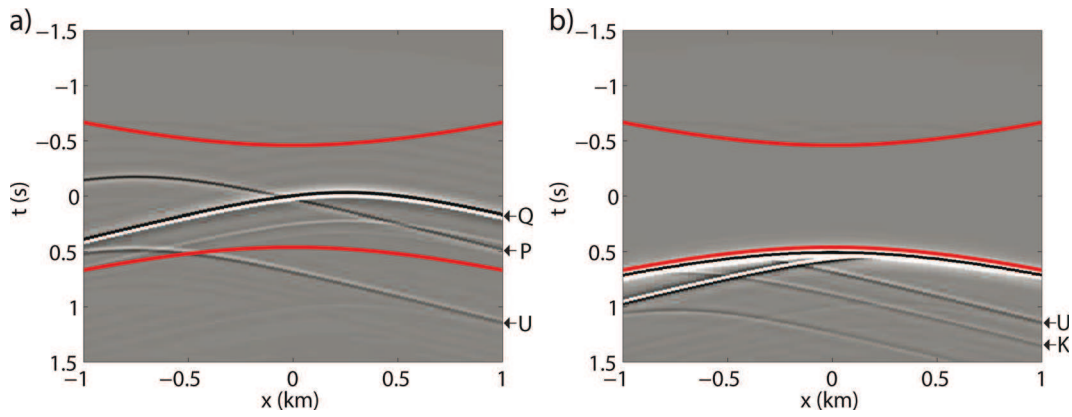


**Figure 26.** (a) Gather of  $Rf_{1d}^+$ . Events P, Q and U are indicated. (b) Retrieved Green's function after two iterations (the upgoing and downgoing parts have been added together). Events U and K are indicated. The red curves define the muting times for matrix  $\Theta$ .

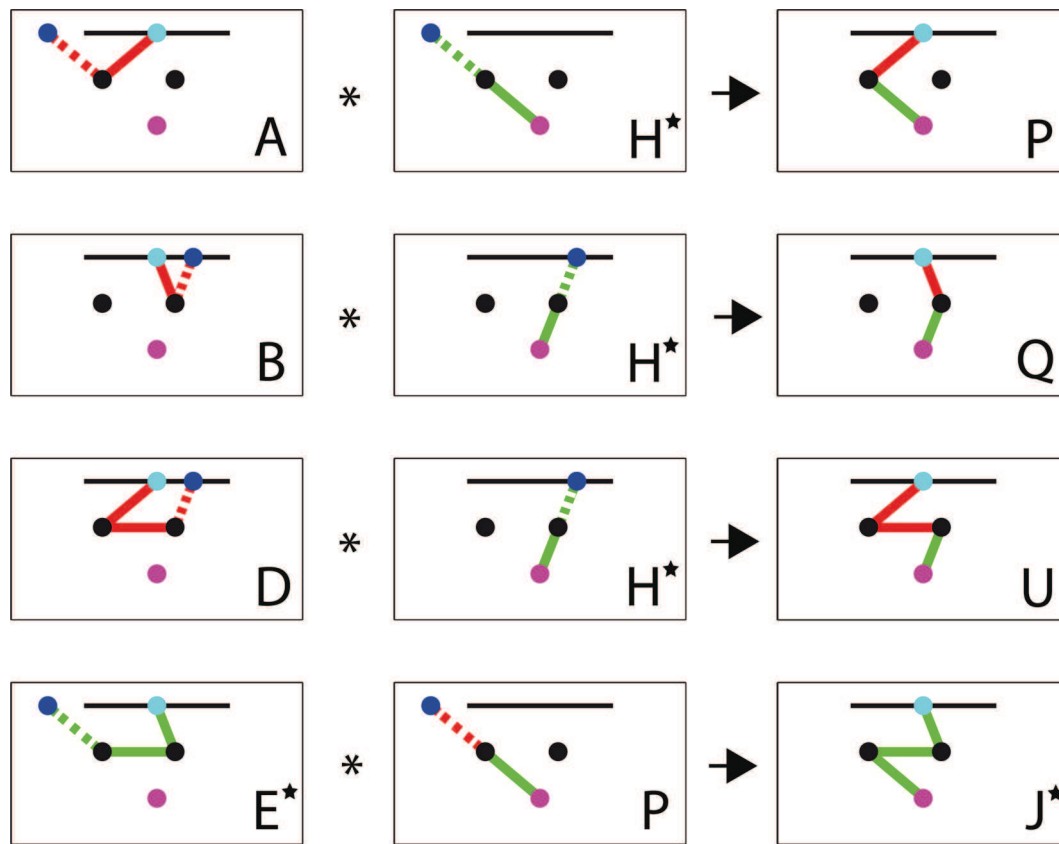


**Figure 27.** Illustrations of the retrieval of events P, Q and U during step 1. In each case, the time-reversed (indicated by superscript  $\star$ ) event  $H^\star$  is convolved with an event in the reflection response. In the lowest panels, we illustrate how the time-reversed downgoing event  $J^\star$  would be constructed during step 2. Since the stationary point  $\mathbf{x}_{XF}$  is not covered by the acquisition array (which is indicated by the solid black line) and event P is poorly retrieved during step 1, this construction cannot be realized.

We also focus our attention to event U that clearly intersects with the lower red curve in Fig. 26(a), representing the muting time for matrix  $\Theta$  that should be applied to this gather to retrieve the initial estimate of  $f_1^-$ . Because of this intersection, the tail of event U is removed by the window matrix, even though it is part of the upgoing focusing function. Besides from not being able to recover the complete focusing function, the tail of U will create an artefact in the estimate of  $g^-$ , since it maps outside the red curves. This artefact will not be removed during higher-order iterations. To understand this problem, we study the way in which event U is constructed, which is illustrated in Fig. 27. This construction involves subtracting

the traveltime from  $\mathbf{x}_Y$  to the focal point from the traveltime from the surface to  $\mathbf{x}_Y$  via  $\mathbf{x}_X$ . Since  $\mathbf{x}_Y$  has a significant lateral separation from  $\mathbf{x}_X$ , the traveltime of event U (0.75 s at  $x = 0$  km) exceeds the traveltime of the direct wave (0.5 s at  $x = 0$  km). Hence, event U maps partly below the red curve at  $x = 0$  km (and various other surface locations) in Fig. 26(a), thereby violating eq. (28). Even though the consequence of this type of imperfection needs further investigation, it is clear that the exact Green's function cannot be retrieved by the current iterative scheme in this case.

To illustrate these limitations, we have retrieved the Green's function (after evaluation of steps 1 and 2). The total Green's function

is constructed by adding its downgoing and upgoing parts together, see Fig. 26(b). Comparing this result with Fig. 25(b), we observe that various events have been retrieved well. However, we also observe the truncated tail of event U, which was part of the retrieved upgoing Green's function. Event J, which appears in Fig. 25(b), is absent in Fig. 26(b). This can be understood from Fig. 27, where we show that event P is required for the retrieval of this event and that stationary point  $\mathbf{x}_{XF}$  should be covered by the acquisition array. Since event P is poorly reconstructed and  $\mathbf{x}_{XF}$  is missed again, event J is not (or barely) visible in the result. We also point at event K in Fig. 26(b), being the wavefield that forward-scattered at  $\mathbf{x}_X$  through a similar mechanism as explained in Fig. 21 (for a different model). Since every point at the surface is stationary for this operation and the acquisition array has been truncated, the amplitude of event K is relatively small. As mentioned earlier, the forward-scattered wavefield (including event K) is a constituent of the direct wavefield under our current definition. Hence, it should have been included in the computation of the initial focusing function, which has not been done in this example. The exact consequences of this violation require further research.

## 6 DISCUSSION

In this paper, we have demonstrated how individual events in the upgoing and downgoing Green's functions are retrieved by iterative substitution of the coupled Marchenko equations. This demonstration provides us a better understanding of this methodology and its limitations. As in seismic interferometry (Schuster 2009), the evaluated integrals contain stationary points that should be sampled by the acquisition array at the surface in order to retrieve particular events of the focusing functions and Green's functions. Successful retrieval is not always guaranteed. As an example, we point at the retrieval of event S, as illustrated in the upper panel of Fig. 21. From this schematic, it is clear that stationary point  $\mathbf{x}_{XY}$  (which we defined in Fig. 16a) should be sampled. If  $\mathbf{x}_X$  and  $\mathbf{x}_Y$  would be located at the same depth level, this stationary point would map at infinity, obstructing the accurate retrieval of event S under any practical condition. In other cases, such as for the construction of event U in the upper panel of Fig. 23, every point at the surface is stationary. Hence, exact amplitudes of this event can never be retrieved with a finite recording aperture. Also seismic attenuation, which is not accounted for in Marchenko redatuming, is likely to cause mismatch in the updates of the focusing functions and Green's functions, when the iterative scheme is applied in practice.

To overcome some of these practical limitations, we may develop an adaptive scheme, where we enforce retrieved events to match. Here, it is important to realize that the upgoing and downgoing constituents of the Green's function are retrieved in a fundamentally different way. For the downgoing Green's function, amplitude updates of physical events are generated at every iteration, as illustrated by Broggini *et al.* (2014b). For the upgoing Green's function, however, all physical events are retrieved with the correct amplitude at the first iteration, whereas later iterations have no other role than to eliminate artefacts. This statement can be validated by the following arguments. To retrieve a physical upgoing event X from event Y in the reflection response, event Y should be propagated backward in time by an event Z in the focusing function. To facilitate this, event Z should have a traveltimes that is less or equal to the traveltimes of the time-reversed direct wave (which is the minimum time to traverse the overburden). Since eq. (27) states that all events in  $\mathbf{f}_{lm}^+$  appear after the time-reversed direct wave, they can never

contribute to the retrieval of any physical upgoing event. Therefore, all physical upgoing events are retrieved by the actions of  $\mathbf{R}$  on the initial focusing function, which happens at the first iteration. Since the only role of the later iterations is the elimination of artefacts, the individual terms in eq. (36) can be summed adaptively, while posing a minimum-energy criterion on the upgoing Green's function  $\mathbf{g}^{-(K)}$ . In free-surface multiple elimination, similar adaptive filters have proven to be of great help in matching predicted events (multiples) to field observations (Verschuur & Berkhout 1997). Applications of adaptive filters for retrieval of the upgoing wavefield have been presented by Van der Neut *et al.* (2015a), using synthetic data, and by Van der Neut *et al.* (2015b), using field data. In both cases, artefacts of internal multiples could be adaptively subtracted from conventional seismic images. Care should be taken, though, since the minimum-energy criterion is not always satisfied when different events are interfering. This is also a common problem in free-surface multiple elimination (Van Borselen *et al.* 2003).

A more fundamental limitation of the current iterative scheme is that the causality conditions that lay at its core can easily be broken. From our observations in media with point scatterers, we note that the apices of most events in the upgoing focusing functions are located in between the red curves, while another part of these events maps outside these curves. Hence, it may be worthwhile to investigate if window matrix  $\Theta$  could be replaced by an alternative filter, potentially in a domain where the separation of the upgoing focusing function and Green's function is more pronounced.

Our observations have important consequences for imaging in complex media. Depending on the recording geometry, Green's function retrieval can be incomplete as particular multiples will simply not be retrieved. From our interferometric interpretation, we can learn that to retrieve an event that arrives at focal point  $\mathbf{x}_F$  with ray parameter  $p$ , this focal point should be visited by the direct wavefield with this specific ray parameter. Hence, it seems virtually impossible to image shadow zones in the subsurface with the current iterative scheme, given that the shadow zone cannot be imaged with primary reflections under a particular recording geometry. However, within the aperture of the direct wavefield, we can retrieve internal multiples. This correct handling of multiple scattering is highly relevant to improve amplitudes and to remove artefacts in depth imaging and inversion, see also Vasconcelos *et al.* (2014b).

Another point of attention is that accurate preprocessing should be carried out before the iterative scheme can be applied. Data should be deghosted at the source and receiver side, free-surface multiples should be removed, the source signature should be deconvolved and the amplitudes should be accurately scaled. For details on this scaling, see Wapenaar *et al.* (2014b) and Van der Neut *et al.* (2015b). To fulfil all these requirements, we could use the output of inversion-based methods that are sometimes applied for free-surface multiple removal. We mention the Up/Down Deconvolution method of Amundsen *et al.* (2001), its implementation for towed-streamer data (Majdanski *et al.* 2011) and estimation of primaries by sparse inversion (Van Groenestijn & Verschuur 2009; Lin & Herrmann 2013). Unlike in the conventional surface-related multiple elimination methodology (Verschuur *et al.* 1992), the source signature is deconvolved by these methods and the appropriate scaling of the output reflection response (as required by our scheme) is guaranteed. To avoid such sophisticated preprocessing, we may also rely on an adaptive Marchenko redatuming scheme (Van der Neut *et al.* 2015a), where we enforce the data to match within a particular degree of freedom that is controlled by the adaptive filter length.

The retrieved upgoing and downgoing Green's functions can be used for seismic imaging with internal multiple reflections (Wapenaar *et al.* 2014a). Based on the previous observations, limitations are to be expected in cases with steeply dipping structures, unless the relevant high ray parameters are included in the initial focusing functions. However, at this point it is unclear how the scheme will behave when the initial focusing functions contain events that propagate close to horizontal or even upgoing arrivals (i.e. diving waves). For these reasons, more research is required in media with strong velocity variations, including media with triplications. It is worth mentioning that good results have been reported by Wapenaar *et al.* (2014b) on applying the iterative scheme with an initial focusing function that includes triplications.

Especially modern nonlinear imaging methods that go beyond the classical single-scattering assumption (also known as the Born approximation) are likely to benefit from the retrieval of Green's functions through the coupled Marchenko equations. These methods often require the computation of multiply scattered wavefields, either through multiple interactions with a model of the medium perturbations (Malcolm *et al.* 2011; Fleury 2013) or by constructing these wavefields in a recursive manner (Berkhout 2012; Davydenko & Verschuur 2014). Since the coupled Marchenko equations provide a linear map between the initial focusing function in a background model and the multiply scattered wavefields in the physical subsurface, they may be an attractive alternative for these computations. As the wavefield can be estimated at any focal point independently, the Marchenko equations seem especially interesting for target-oriented approaches. The Marchenko equations can also be useful to obtain a reflection response at the bottom of a seismic (sub)volume to turn recorded data with one-sided illumination into new data with two-sided illumination. Such an attempt could be highly relevant for nonlinear imaging, since a lack of illumination from below is known to limit its potential (Fleury & Vasconcelos 2012; Ravasi *et al.* 2014). To obtain reflection responses from below, we could either invert eq. (12) at a single focusing level (Wapenaar *et al.* 2014a) or make use of a target-enclosing redatuming scheme that was recently presented by Van der Neut *et al.* (2013).

## 7 CONCLUSIONS

Inverse wavefield extrapolation can be interpreted as applying a multidimensional filter of time-reversed Green's functions to seismic reflection data. These time-reversed Green's functions are typically computed in a macro velocity model and can be interpreted as initial focusing functions. Scattering is not accounted for by this approach. Inverse wavefield extrapolation can also be interpreted as applying a multidimensional filter of reflection data to an initial focusing function. This filter propagates the initial focusing function forward in time with the reflection response. In Green's function retrieval by iterative substitution of the coupled Marchenko equations, scattering effects are taken into account by applying a more complicated filter to the initial focusing function. This filter involves a linear combination of several successive operations that include propagating the wavefield forward in time with the reflection response, truncating it to impose particular causality criteria and propagating it backward in time with the reflection response. Separate filters can be defined for the upgoing and downgoing Green's functions. Each operation that involves propagation (forward or backward in time) with the reflection response can be interpreted as a multidimensional cross-correlation process. This process can be analysed by subtracting traveltimes along common ray paths at the stationary points of the

underlying integrals. In this way, the retrieval of individual events can be visualized.

From this interpretation, it follows that the downgoing and upgoing Green's functions are retrieved in a fundamentally different way. For the downgoing Green's function, the amplitudes of physical events are updated at every iteration. For the upgoing Green's function, all physical events are retrieved with correct amplitudes at the first iteration. Later iterations, however, are required to eliminate artefacts. To retrieve a specific down- or upgoing event, particular stationary points should be sampled at the surface. For some events, every surface location is stationary. This poses limitations to what can be retrieved and to the amplitude recovery of particular events in case of a finite recording aperture. Moreover, to retrieve an internal multiple at a particular subsurface location with a particular ray parameter, the direct wavefield should visit this specific location with this specific ray parameter. Finally, it is observed that the causality criteria that undergird the Marchenko equations are not always obeyed in complex media, which can lead to artefacts in the retrieved Green's functions. Despite these limitations, the Marchenko methodology can be highly relevant for handling multiple scattering in depth imaging and several encouraging results of this approach have been presented recently.

## ACKNOWLEDGEMENTS

This research is financially supported by the Dutch Technology Foundation STW, applied science division of NWO and the technology program of the Ministry of Economic Affairs (grant VENI.13078). We thank Jan Thorbecke, Evert Slob (Delft University of Technology), Filippo Brogini, Dirk-Jan van Manen (ETH Zürich), Roel Snieder, Satyan Singh (Colorado School of Mines), Pablo David García López (University of Oviedo), James Rickett, Colin Thomson (Schlumberger Gould Research), Yi Liu (Norwegian University of Science and Technology) and Matteo Ravasi (University of Edinburgh) for fruitful discussions that contributed to this paper.

## REFERENCES

- Al-Ali, M.N. & Verschuur, D.J., 2006. An integrated method for resolving the seismic complex near-surface problem, *Geophys. Prospect.*, **54**(6), 739–750.
- Amundsen, L., Ikelle, T. & Berg, L.E., 2001. Multidimensional signature deconvolution and free-surface multiple elimination of marine multicomponent ocean-bottom seismic data, *Geophysics*, **66**(5), 1594–1604.
- Bakulin, A. & Calvert, R., 2006. The virtual source method: theory and case study, *Geophysics*, **71**(4), S1139–S1150.
- Behura, J., Wapenaar, K. & Snieder, R., 2014. Autofocus imaging: image reconstruction based on inverse scattering theory, *Geophysics*, **79**(3), A19–A26.
- Berkhout, A.J., 2012. Combining full wavefield migration and full waveform inversion, a glance into the future of seismic imaging, *Geophysics*, **77**(2), S43–S50.
- Berryhill, J.R., 1984. Wave-equation datuming before stack, *Geophysics*, **49**(8), 2064–2066.
- Brogini, F. & Snieder, R., 2012. Connection of scattering principles: a visual and mathematical tour, *Eur. J. Phys.*, **33**, 593–613.
- Brogini, F., Snieder, R. & Wapenaar, K., 2014a. Data-driven wave field focusing and imaging with multidimensional deconvolution: numerical examples from reflection data with internal multiples, *Geophysics*, **79**(3), WA107–WA115.
- Brogini, F., Wapenaar, K., van der Neut, J. & Snieder, R., 2014b. Data-driven Green's function retrieval and application to imaging with multidimensional deconvolution, *J. geophys. Res.*, **119**, 425–444.

- Corones, J.P., Davison, M.E. & Krueger, R.J., 1983. Direct and inverse scattering in the time domain via invariant imbedding equations, *J. acoust. Soc. Am.*, **74**, 1535–1541.
- da Costa Filho, C., Ravasi, M., Curtis, A. & Meles, G., 2014. Elastodynamic Green's function retrieval through single-sided Marchenko inverse scattering, *Phys. Rev. E*, **90**(6), doi:10.1103/PhysRevE.90.063201.
- Davydenko, M. & Verschuur, D.J., 2014. Full wavefield migration in three dimensions, in *84th Annual Meeting, SEG, Expanded Abstracts*. SEG, Tulsa, OK, pp. 3935–3940.
- De Bruin, C.G.M., Wapenaar, C.P.A. & Berkhout, A.J., 1990. Angle-dependent reflectivity by means of prestack migration, *Geophysics*, **55**(9), 1223–1234.
- Fishman, L., McCoy, J.J. & Wales, S.C., 1987. Factorization and path integration of the Helmholtz equation: numerical algorithms, *J. acoust. Soc. Am.*, **81**, 1355–1376.
- Fleury, C., 2013. Increasing illumination and sensitivity of reverse-time migration with internal multiples, *Geophys. Prospect.*, **61**(5), 891–906.
- Fleury, C. & Vasconcelos, I., 2012. Imaging condition for nonlinear scattering-based imaging: estimate of power loss in scattering, *Geophysics*, **77**(1), S1–S18.
- Fokkema, J.T. & Van den Berg, P.M., 1993. *Seismic Applications of Acoustic Reciprocity*, Elsevier Science Pub. Co.
- Frijlink, M. & Wapenaar, K., 2010. Reciprocity theorems for one-way wave fields in curvilinear coordinate systems, *SIAM Journal on Imaging Sciences*, **3**(3), 390–415.
- Galetti, E., Halliday, D. & Curtis, A., 2013. A simple and exact acoustic wavefield modeling code for data processing, imaging, and interferometry applications, *Geophysics*, **78**(6), F17–F27.
- Ikelle, L.T., 2006. A construct of internal multiples from surface data only: the concept of virtual seismic events, *Geophys. J. Int.*, **164**, 383–393.
- Ikelle, L.T. & Gangi, A.F., 2007. Negative bending in seismic reflection associated with time-advanced and time-retarded fields, *Geophys. Prospect.*, **55**(1), 57–69.
- Jakubowicz, H., 1998. Wave equation prediction and removal of interbed multiples, in *68th EAGE Conference and Exhibition, Extended Abstracts*, pp. 1527–1530, doi:10.3997/2214-4609.201408173.
- Lin, T.T.Y. & Herrmann, F.J., 2013. Robust estimation of primaries by sparse inversion via one-norm minimization, *Geophysics*, **78**(3), R133–R150.
- Majdanski, M., Kostov, C., Kragh, E., Moore, I., Thompson, M. & Mispel, J., 2011. Attenuation of free-surface multiples by up/down deconvolution for marine towed-streamer data, *Geophysics*, **76**(6), V129–V138.
- Malcolm, A.E., de Hoop, M.V. & Calandra, H., 2007. Identification of image artifacts from internal multiples, *Geophysics*, **72**(2), SI23–SI32.
- Malcolm, A.E., de Hoop, M.V. & Ursin, B., 2011. Recursive imaging with multiply scattered waves using partial image regularization: a north sea case study, *Geophysics*, **76**(2), 33–42.
- Mehta, K., Bakulin, A., Sheiman, J., Calvert, R. & Snieder, R., 2007. Improving the virtual source method by wavefield separation, *Geophysics*, **72**(4), V79–V86.
- Mehta, K., Snieder, R., Calvert, R. & Sheiman, J., 2008. Acquisition geometry requirements for generating virtual-source data, *Leading Edge*, **27**, 620–629.
- Meles, G., Løer, K., Ravasi, M., Curtis, A. & da Costa Filho, C.A., 2015. Internal multiple prediction and removal using Marchenko autofocusing and seismic interferometry, *Geophysics*, **80**(1), A7–A11.
- Ravasi, M. & Curtis, A., 2012. Nonlinear scattering based imaging in elastic media: theory, theorems and imaging conditions, *Geophysics*, **78**(3), S137–S155.
- Ravasi, M., Vasconcelos, I. & Curtis, A., 2014. Beyond conventional migration: non-linear elastic subsalt imaging with transmissions and two-sided illumination, *Geophys. J. Int.*, **198**, 1187–1199.
- Ravasi, M., Vasconcelos, I., Kritski, A., Curtis, A., da Costa Filho, C. & Meles, G.A., 2015. Marchenko imaging of Volve Field, North Sea, in *77th EAGE Conference and Exhibition, Extended Abstracts*, doi:10.3997/2214-4609.201412938.
- Rose, J., 2002. Single-sided autofocusing of sound in layered materials, *Inverse Probl.*, **18**, 1923–1934.
- Sava, P. & Vasconcelos, I., 2011. Extended imaging condition for wave-equation migration, *Geophys. Prospect.*, **59**(1), 35–55.
- Schuster, G.T., 2009. *Seismic Interferometry*, Cambridge Univ. Press.
- Singh, S., Snieder, R., Behura, J., van der Neut, J., Wapenaar, K. & Slob, E., 2015. Autofocus imaging: imaging with primaries, internal multiples and free-surface multiples, *Geophysics*, **80**(4), S165–S174.
- Slob, E., Wapenaar, K., Broggini, F. & Snieder, R., 2014. Seismic reflector imaging using internal multiples with Marchenko-type equations, *Geophysics*, **79**(2), S63–S76.
- Snieder, R., Wapenaar, K. & Larner, K., 2006. Spurious multiples in seismic interferometry of primaries, *Geophysics*, **71**(4), S1111–S1124.
- Tenkroode, P.E., 2002. Prediction of internal multiples, *Wave Motion*, **35**, 315–338.
- Thomson, C., 2012. The form of the reflection operator and extended image gathers for a dipping plane reflector in two space dimensions, *Geophys. Prospect.*, **60**(1), 64–92.
- Van Borselen, R.G., Fookes, G. & Brittan, J., 2003. Target-oriented adaptive subtraction in data-driven multiple removal, *Leading Edge*, **22**, 340–343.
- Van der Neut, J., Almagro Vidal, C., Grobbe, N. & Wapenaar, K., 2013. Turning one-sided illumination into two-sided illumination by target-enclosing interferometric redatuming, in *75th EAGE Conference and Exhibition, Extended Abstracts*, doi:10.3997/2214-4609.20130190.
- Van der Neut, J., Wapenaar, K., Slob, E. & Vasconcelos, I., 2015a. An illustration of adaptive Marchenko imaging, *Leading Edge*, **34**, 818–822.
- Van der Neut, J., Wapenaar, K., Thorbecke, J. & Slob, E., 2015b. Practical challenges in adaptive Marchenko imaging, in *85th Annual Meeting, SEG, Expanded Abstracts*, New Orleans, LA.
- Van Groenestijn, G.J.A. & Verschuur, D.J., 2009. Estimation of primaries and near-offset reconstruction by sparse inversion: marine data applications, *Geophysics*, **74**(3), R119–R128.
- Vasconcelos, I. & Rickett, J., 2013. Broadband extended images from joint inversion of multiple blended wavefields, *Geophysics*, **78**(2), WA147–WA158.
- Vasconcelos, I., Ravasi, M. & van der Neut, J., 2014a. An interferometry-based, subsurface-domain objective function for targeted waveform inversion, *76th EAGE Conference and Exhibition, Extended Abstracts*, doi:10.3997/2214-4609.20141090.
- Vasconcelos, I., van Manen, D.J., Ravasi, M., Wapenaar, K. & van der Neut, J., 2014b. Marchenko redatuming: advantages and limitations in complex media, *Workshop W-11, 84th Annual Meeting, SEG, Expanded Abstracts*, SEG, Denver, CO.
- Verschuur, D.J. & Berkhout, A.J., 1997. Estimation of multiple scattering by iterative inversion, part II: Practical aspects and examples, *Geophysics*, **62**(9), 1595–1611.
- Verschuur, D.J., Berkhout, A.J. & Wapenaar, C.P.A., 1992. Adaptive surface-related multiple elimination, *Geophysics*, **57**(5), 1166–1177.
- Wapenaar, C.P.A. & Grimbergen, J.L.T., 1996. Reciprocity theorems for one-way wavefields, *Geophys. J. Int.*, **127**, 169–177.
- Wapenaar, K. & Slob, E., 2014. On the Marchenko equation for multicomponent single-sided reflection data, *Geophys. J. Int.*, **199**, 1367–1371.
- Wapenaar, K., Slob, E. & Snieder, R., 2010. On seismic interferometry, the generalized optical theorem and the scattering matrix of a point scatterer, *Geophysics*, **75**, SA27–SA35.
- Wapenaar, K., Van der Neut, J., Ruigrok, E., Draganov, D., Hunziker, J., Slob, E., Thorbecke, J. & Snieder, R., 2011. Seismic interferometry by crosscorrelation and by multidimensional deconvolution: a systematic comparison, *Geophys. J. Int.*, **185**, 1335–1364.
- Wapenaar, K., Thorbecke, J., van der Neut, J., Broggini, F., Slob, E. & Snieder, R., 2014a. Marchenko imaging, *Geophysics*, **79**(3), WA39–WA57.
- Wapenaar, K., Thorbecke, J., van der Neut, J., Broggini, F., Slob, E. & Snieder, R., 2014b. Green's function retrieval from reflection data, in absence of a receiver at the virtual source position, *J. acoust. Soc. Am.*, **135**(5), 2847–2861.
- Weglein, A.B., Gasparotto, F.A., Carvalho, P.M. & Stolt, R.H., 1997. An inverse-scattering series method for attenuating multiples in seismic reflection data, *Geophysics*, **12**, 1975–1989.